© 2020. Published by The Company of Biologists Ltd | Development (2020) 147, dev188052. doi:10.1242/dev.188052

RESEARCH ARTICLE

The FOXJ1 target *Cfap206* is required for sperm motility, mucociliary clearance of the airways and brain development

Anja Beckers[1,¶], Christian Adis[1,*,¶], Karin Schuster-Gossler[1], Lena Tveriakhina[1], Tim Ott[2], Franziska Fuhl[2], Jan Hegermann[3], Karsten Boldt[4], Katrin Serth[1], Ev Rachev[1], Leonie Alten[1,‡], Elisabeth Kremmer[5,§], Marius Ueffing[4], Martin Blum[2,] and Achim Gossler[1,**]**

ABSTRACT

Cilia are complex cellular protrusions consisting of hundreds of proteins. Defects in ciliary structure and function, many of which have not been characterised molecularly, cause ciliopathies: a heterogeneous group of human syndromes. Here, we report on the FOXJ1 target gene *Cfap206*, orthologues of which so far have only been studied in *Chlamydomonas* and *Tetrahymena*. In mouse and *Xenopus*, *Cfap206* was co-expressed with and dependent on *Foxj1*. CFAP206 protein localised to the basal body and to the axoneme of motile cilia. In *Xenopus* crispant larvae, the ciliary beat frequency of skin multiciliated cells was enhanced and bead transport across the epidermal mucociliary epithelium was reduced. Likewise, *Cfap206* knockout mice revealed ciliary phenotypes. Electron tomography of immotile knockout mouse sperm flagella indicated a role in radial spoke formation reminiscent of FAP206 function in *Tetrahymena*. Male infertility, hydrocephalus and impaired mucociliary clearance of the airways in the absence of laterality defects in *Cfap206* mutant mice suggests that *Cfap206* may represent a candidate for the subgroup of human primary ciliary dyskinesias caused by radial spoke defects.

KEY WORDS: Motile cilia, Hydrocephalus, Male infertility, Mucus accumulation, Radial spoke defect, Ciliary beat frequency

INTRODUCTION

Cilia are projections found on the surface of many eukaryotic cells. They are essential for development and adult tissue homeostasis. Cilia can be non-motile (or sensory) or motile, and cells can carry a single (motile or immotile) cilium or up to several hundred motile cilia (Takeda and Narita, 2012). The ciliary core, the axoneme, consists of nine peripheral microtubular doublets and may or may not possess a central pair of single microtubules. Cilia consist of hundreds of proteins, many of which are common to non-motile and motile cilia (Arnaiz et al., 2009; Gherman et al., 2006; Inglis et al., 2006). Non-motile cilia often sense environmental cues, whereas motile cilia move extracellular fluids or mediate cell motility. In early fish, amphibian and mammalian embryos, the rotation of single motile cilia of left-right organizer cells (LRO) generates a leftward fluid flow in the extracellular space. The resulting left-asymmetric gene expression establishes left-right asymmetry and drives asymmetric morphogenesis and placement of visceral organs (Blum and Ott, 2018; Hirokawa et al., 2006). Wave-like beating of cilia on airway epithelial multiciliated cells (MCCs) is essential for airway clearance throughout postnatal life (Jain et al., 2010; Stannard and O'Callaghan, 2006). MCCs on ependymal cells lining the brain ventricles are responsible for cerebrospinal fluid movement (Banizs et al., 2005; Jacquet et al., 2009; Lee, 2013; Spassky et al., 2005). Motile cilia in the fallopian tubes contribute to movement of egg and zygote (Lyons et al., 2006), and the sperm flagellum is essential for its motility (Afzelius and Eliasson, 1983). The central pair and its accessory structures, namely radial spokes that connect the central pair to the outer microtubule doublets, are crucial for the planar beating pattern of 9+2 cilia (Shinohara et al., 2015) as well as regulation of dynein motor activity and microtubule sliding (Lindemann and Lesich, 2010; Satir et al., 2014).

The evolutionarily conserved transcription factor FOXJ1 plays a central role in motile ciliogenesis (Choksi et al., 2014). Loss of FOXJ1 leads to non-functional rotating cilia in the LRO of the mouse, the ventral node (Alten et al., 2012), and to complete absence of motile cilia on multiciliated cells (MCCs), such as airway epithelial cells or brain ependyma (Brody et al., 2000; Chen et al., 1998).

Defects in motile ciliary structure and/or function can lead to primary ciliary dyskinesia (PCD, OMIM 244400), a syndrome that affects about 1/10,000-1/15,000 humans (Lucas et al., 2019). PCD is a heterogeneous disorder; patients suffer from recurrent infections of the airways, male sterility, laterality defects in 50% of cases and – more rarely – hydrocephalus (Praveen et al., 2015). Nonsense or frameshift mutations in FOXJ1 that cause an autosomal dominant form of PCD have been identified (Wallmeier et al., 2019), and dysfunction of direct or indirect FOXJ1 targets are implicated in the development of numerous human PCD cases (Mukherjee et al., 2019). In microarray screens, we identified additional cilia-associated target genes of FOXJ1 (Stauber et al., 2017). We have started to evaluate selected evolutionarily conserved candidates by descriptive and loss-of-function analyses in two vertebrate model organisms, the frog *Xenopus laevis* and the mouse. All of these candidates were co-expressed with *Foxj1* throughout embryonic development in mouse and frog, including the LRO (mouse and

[1]Institute for Molecular Biology, OE5250, Hannover Medical School, Carl-Neuberg-Str. 1, 30625 Hannover, Germany. [2]Institute of Zoology, University of Hohenheim, Garbenstraße 30, 70593 Stuttgart, Germany. [3]Institute of Functional and Applied Anatomy, OE8840, Hannover Medical School, Carl-Neuberg-Str. 1, 30625 Hannover, Germany. [4]Institute of Ophthalmic Research, Center for Ophthalmology, University of Tübingen, Röntgenweg 11, 72076 Tübingen, Germany. [5]Institute of Molecular Immunology, Helmholtz Zentrum München, German Research Center for Environmental Health, Core Facility Monoclonal Antibodies, Marchioninistr. 25, 81377 München, Germany.
*Present address: Mediagnost Gesellschaft für Forschung und Herstellung von Diagnostika GmbH, Aspenhaustr. 25, 72770 Reutlingen, Germany. ‡Present address: Twist Bioscience, 681 Gateway Blvd South, South San Francisco, CA 94080. §Present address: Department of Biology II, Ludwig-Maximilians University, Großhaderner Straße 2, 82152 Martinsried, Germany.
¶These authors contributed equally to this work

**Authors for correspondence (martin.blum@uni-hohenheim.de; gossler.achim@mh-hannover.de)

M.B., 0000-0002-4834-1520; A.G., 0000-0002-9103-9116

Handling editor: John Wallingford
Received 10 January 2020; Accepted 15 April 2020

Development (2020) 147, dev188052. doi:10.1242/dev.188052

frog), MCCs of the ependyma (mouse and frog), airways (mouse) and larval skin (frog) as well as sperm cells (mouse). These genes were found to have distinct context- and species-specific functions in motile cilia (Beckers et al., 2018; Weidemann et al., 2016).

Here, we report on the analysis of *Cfap206* as an additional evolutionarily conserved FOXJ1 target gene that so far has only been analysed in single-celled eukaryotes. FAP206, the orthologue of CFAP206 in the green alga *Chlamydomonas*, is a potential component of the nexin-dynein regulatory complex (Lin et al., 2011) and interacts with radial spoke protein 3 (RSP3) (Gupta et al., 2012). FAP206 in the ciliate *Tetrahymena* is required for anchoring radial spoke 2 (RS2) to microtubule doublets and for generating the waveform of ciliary movement (Vasudevan et al., 2015). We show that the vertebrate homolog CFAP206 localises to the basal body/centrosome and to cilia, and its expression correlates with and depends on *Foxj1* expression. Genome editing in *Xenopus* resulted in moderate ciliary defects during larval development, namely slightly increased ciliary beat frequency of epidermal MCCs and slightly impaired bead transport across the skin epithelium. Knockout mice postnatally developed hydrocephalus, revealed impaired mucociliary clearance of the airways and were characterised by male infertility. As in *Xenopus*, CFAP206 loss affected beat frequency of cilia on tracheal MCCs, while sperm were largely immotile. Electron tomographic analysis revealed that CFAP206 was needed to establish the repetitive pattern of RS1, RS2 and RS3 in the sperm flagellum, reminiscent of the function described in *Tetrahymena*. Immotile sperm, impaired mucociliary clearance of the airways and hydrocephalus are hallmarks of PCD. Our analyses of *Cfap206* as a thus far uncharacterised *Foxj1* target therefore indicate that this gene may qualify as a new PCD candidate gene worth studying in human PCD cohorts.

RESULTS

Cfap206 is co-expressed with and dependent on *Foxj1* in mouse and frog

The mouse *Cfap206* gene (http://www.ensembl.org/Mus_musculus/Gene/Summary?db=core;g=ENSMUSG00000028294) gives rise to two transcripts by differential splicing that encode proteins of 622 and 504 amino acids (Fig. 1A). The shorter protein (CFAP206 S) lacks the C-terminal region and is characterised by six unique amino acids at its C-terminus, while the remaining protein is identical to the long variant (CFAP206L). CFAP206 is an evolutionarily conserved protein (Table S1). It lacks known motifs or domains, except for a unique 280 amino acid domain of unknown function with conserved motifs GFC and GIL. Expression analysis of mRNAs by RT-PCR demonstrated that both variants were co-expressed in adult tissues (Fig. 1B). This pattern coincided with *Foxj1*, supporting the identification of *Cfap206* as a target gene (Fig. 1B). *In situ* hybridisation of adult tissue sections using a probe detecting both transcripts (Fig. 1A) revealed mRNA expression in cells carrying motile cilia of the male and female reproductive tract (sperm and oviduct; Fig. 1Ca,a′,b,b′), the airways (lung and nasal cavity; Fig. 1Cc,c′,d,d′) as well as brain ependyma and choroid plexus (CP; Fig. 1Ce,e′). During embryogenesis (E17.5), mRNA was found in airway epithelia (Fig. 1Da-c′) and brain ependymal tissues, i.e. correlated with MCCs (Fig. 1Dd,d′). Early in development, *Cfap206* mRNA was confined to the LRO (ventral node) of 8-day-old embryos (E8.0; Fig. 1Ea). Expression in a number of cell types carrying non-motile cilia was also detected (Figs S1 and S8). The dependence of *Cfap206* expression on the activity of the transcription factor FOXJ1 was analysed in *Foxj1* knockout mice (*Foxj1*$^{-/-}$). *Cfap206* transcripts were severely downregulated or nearly absent in *Foxj1* mutants (Fig. 1E), corroborating that *Cfap206* acts downstream of FOXJ1.

During *Xenopus* embryogenesis, *cfap206* mRNA transcription also paralleled that of *foxj1*, with few exceptions. Prominent *cfap206* signals were seen in the *Xenopus* LRO, i.e. gastrocoel roof plate, the floor plate (FP) of the neural tube, MCCs of the larval skin, the nephrostomes, the branchial chambers (BCs) and the stomach (Fig. 2Af,g,h′,h″), i.e. in cells and tissues that harbour motile cilia. Expression of *foxj1* transcripts were detected in the same tissues (Fig. 2Ab,c,d-d‴) except for the LRO (Fig. 2Ab′; staining in b reflects expression in the FP). *Foxj1* signals, however, were present in the LRO precursor tissue of the superficial mesoderm (SM; Fig. 2Aa), where no *cfap206* signals were found (Fig. 2Ae). In the brain, *foxj1* and *cfap206* were expressed in the zona limitans intrathalamica (ZLI), in the sub-commissural organ (SCO) and in the FP (Fig. 2Ad‴,h‴), where *foxj1* signals were much stronger than those of *cfap206*. Ectopic expression of *foxj1* on one side of the larva, following unilateral injection of synthetic mRNA at the four-cell stage, resulted in strong induction of ectopic *cfap206* transcription on the injected side (asterisk; Fig. 2B). The dependence of *cfap206* transcription on *foxj1* was analysed in specimens that were genome edited at the *foxj1* gene locus by CRIPSR/Cas9 (Rachev et al., 2020). Signal intensities were greatly reduced in crispants (Fig. 2C), corroborating data in the mouse. Together, these experiments in mouse and frog demonstrate that FOXJ1 is the decisive transcription factor for *cfap206* activation in cells carrying motile cilia during embryonic development and likely also for its expression in adult tissues.

CFAP206 localises to the ciliary axoneme and basal body

To study CFAP206 localisation, we generated polyclonal antibodies in rabbits and monoclonal antibodies in rats. One polyclonal antibody was directed against a peptide (pepI: amino acids 194-207; encoded by exon 6; green box Fig. 3A) present in both protein variants, a second one was specific for the long CFAP206 protein (pepII: amino acids 576-589; encoded by exon 13; orange box Fig. 3A). Both polyclonal antibodies detected Flag- or GFP-tagged CFAP206 overexpressed in CHO cells (Fig. 3A). The monoclonal antibodies were directed against a peptide largely overlapping with pepII (ORF2:amino acids 574-586; cyan box Fig. 3A) and therefore also specific for the long CFAP206 protein variant. Endogenous CFAP206 protein was detected in western blots of testis lysates (Fig. 3A) as well as in cell lines carrying non-motile cilia (Fig. S1C). As the α-pepI antibodies gave rise to high background in immunofluorescence staining, the subcellular localisation of CFAP206 was assessed using the long form-specific α-pepII antibody on sections of the nasal respiratory epithelium and adult mouse testis (Fig. 3B). In motile cilia of the adult nasal respiratory epithelium, CFAP206 staining largely overlapped with acetylated-α-tubulin (ac-TUB). Signals were also detected proximally to ac-TUB (arrowheads in Fig. 3Bd,d′), reflecting a potential localisation at basal bodies, which was clearly observed in mIMCD3 cells (Fig. S1Da-d). No clear overlap of CFAP206 staining with ac-TUB was observed at the distal tip of cilia (arrows in Fig. 3Bd,d′), suggesting that CFAP206 was present throughout the axoneme except for the tip region. In spermatozoa CFAP206 was co-detected with ac-TUB in the flagella (Fig. 3Be-g). Expression in differentiating spermatids was found from the earliest stages of spermiogenesis onwards (Fig. S2).

In *Xenopus*, the polyclonal rabbit antibodies (pepI and pepII) against mouse CFAP206 did not give rise to any staining (not shown). In order to assess ciliary localisation in an indirect manner,

Development (2020) 147, dev188052. doi:10.1242/dev.188052

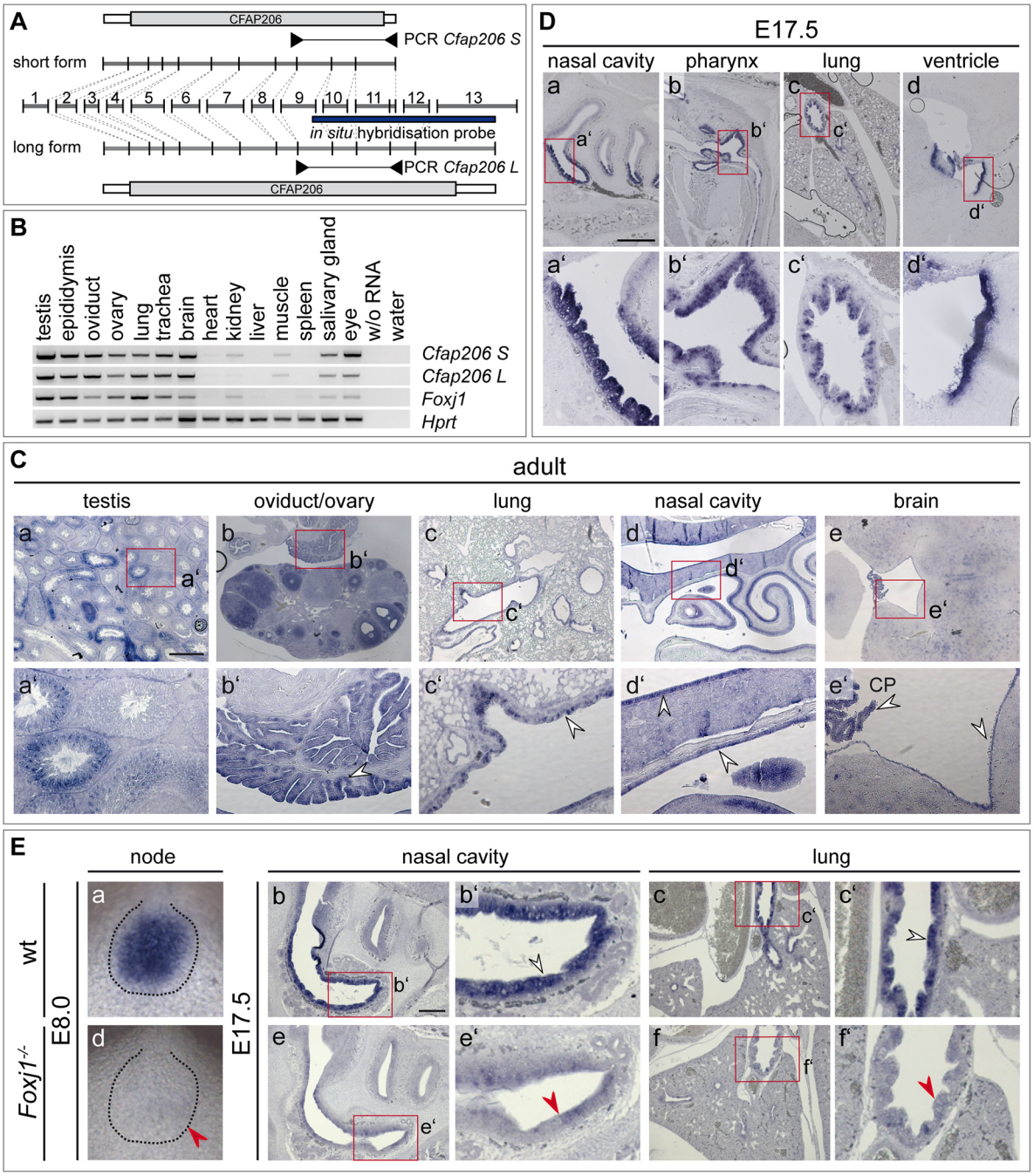

Fig. 1. The structure of the mouse *Cfap206* and *Cfap206* expression. (A) Schematic depiction of the *Cfap206* genomic structure, transcripts and resulting proteins. The *Cfap206* gene consists of 13 exons (middle row) that give rise to two transcripts: a short form (*Cfap206 S*; upper row) and a long form (*Cfap206 L*; lower row), generated by the differential use of a splice donor site in exon 11. Grey boxes indicate ORFs, white boxes indicate the 5′- and 3′-UTR. PCR *Cfap206 S* and PCR *Cfap206 L* indicate the position of primers and PCR products used to distinguish between both transcripts. Blue box marks the region used to generate the *in situ* hybridisation probe, which detected both transcripts. (B) Correlation of *Cfap206 S*, *Cfap206 L* and *Foxj1* expression in adult tissues assessed by RT-PCR. *Hprt* was used as quality control. The full-size agarose gel is shown in Fig. S7. (C) Expression of *Cfap206* in adult tissues detected by section *in situ* hybridisation. Boxed areas in a-e indicate the regions shown at higher magnification in a′-e′. Arrowheads indicate regions of expression. CP, choroid plexus. (D) Expression of *Cfap206* in tissues developing or carrying motile cilia at E17.5 detected by section *in situ* hybridisation. Boxed areas in a-d indicate the regions shown at higher magnification in a′-d′. (E) Dependence of *Cfap206* expression on FOXJ1. Whole-mount *in situ* hybridisation (a,d) and section *in situ* hybridisation (b,c,e,f) on wild-type (a-c) and *Foxj1* mutant (d-f) E8.0 embryos (a,d), and E17.5 nasal cavities (b,e) and lungs (c,f). Red boxes in b,c,e,f indicate regions enlarged in b′,c′,e′,f′. *Cfap206* expression was reduced or nearly absent in the mouse left-right organiser (LRO), the respiratory epithelium and bronchi of *Foxj1* mutants (red arrowheads in d,e′,f′). Scale bars: 500 µm in C,D; 200 µm in Eb,c,e,f.

fusion proteins were expressed by targeted injection of mRNAs into the epidermal lineage at the two- to four-cell stage. A GFP-fusion protein with murine CFAP206 was used (GFP-CFAP206), which – when injected at high levels – labelled defined spherical structures throughout the cell, resembling previously described liquid-like organelles (not shown; Huizar et al., 2018) (Fig. 3C).

Development (2020) 147, dev188052. doi:10.1242/dev.188052

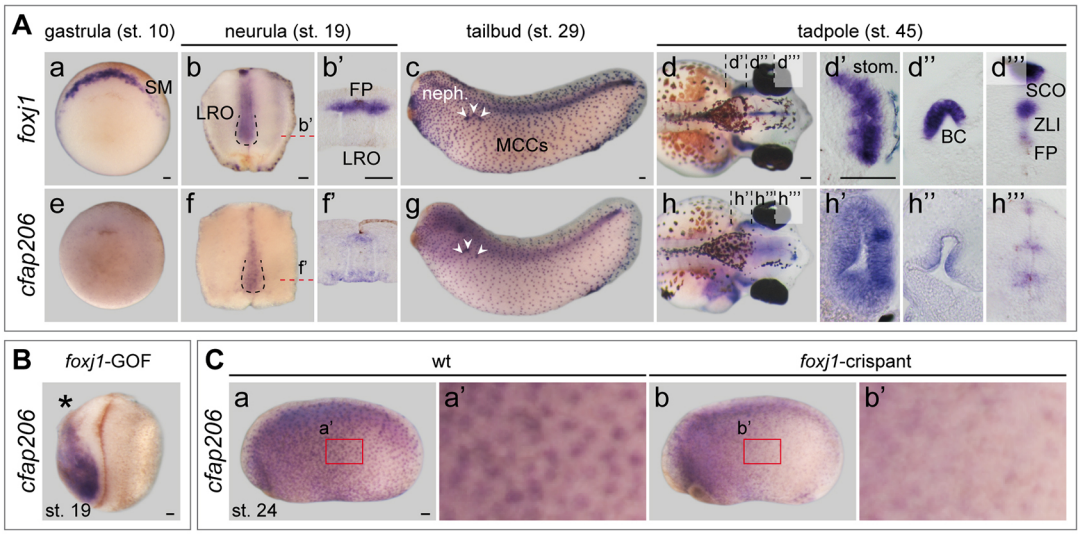

Fig. 2. *cfap206* is co-expressed with and dependent on *foxj1* in *Xenopus laevis*. (A) Analysis of *foxj1* and *cfap206* mRNA expression in staged embryos using antisense RNA probes. (a,e) In gastrula stage 10 embryos, *foxj1* transcripts were present in the LRO precursor, the superficial mesoderm (SM; a), while *cfap206* was not detected by *in situ* hybridisation (e). Histological sections (b′,f′; planes of sections indicated by red dashed lines in b,f) of stage 19 dorsal explants (b,f) revealed overlapping expression of *foxj1* (b,b′) and *cfap206* (f,f′) in the floor plate (FP), while in the gastrocoel roof plate (area of LRO; outlined by dashed lines in b,f), only *cfap206* transcripts were detected. Staining in b reflects expression in the floorplate above the LRO. (c,g) In stage 29 larvae, both genes were co-expressed in the nephrostomes (white arrowheads) and MCCs. (d,h) In the head of stage 45 tadpoles, strong neural expression of *foxj1* was seen in the sub-commissural organ (SCO), zona limitans intrathalamica (ZLI) and FP (d‴). Transcripts of *cfap206* were detected in the same tissues; however, at reduced levels (h‴). Non-neural expression was found in the stomach (stom.; d′,h′) and in dorsal cells lining the branchial chamber (BC; d″,h″). (B,C) *cfap206* is a *foxj1* target gene. (B) Strong *cfap206* induction in embryos unilaterally injected with *foxj1* mRNA. Asterisk indicates injected side. (C) Reduction of *cfap206* expression in stage 24 *foxj1* F0 crispant embryos (b,b′) when compared with wild type (a,a′). Boxed areas in a,b indicate the regions shown at higher magnification in a′,b′. Scale bars: 100 µm.

GFP-CFAP206 partially overlapped with RFP-tagged centrin 4 (Cetn4-RFP) (Cetn4; Zhang and Mitchell, 2016) at basal bodies of epidermal MCCs (Fig. 3Ca). The orthogonal projection depicted in Fig. 3Ca′ revealed a defined succession of domains, with proximal (i.e. closest to the axoneme) centrin 4 staining, followed by a small zone of centrin 4-CFAP206 overlap and a distal CFAP206 domain. Basal body localisation was confirmed by co-staining of GFP-CFAP206 with the basal foot marker tubulin γ1 (Tubg1; Fig. 3Cb). GFP-CFAP206 partially overlapped with Tubg1, both in the plane parallel to the cell surface (Fig. 3Cb′) as well as in an orthogonal projection (Fig. 3Cb″), where GFP-CFAP206 extended towards the distal end of the basal body, at the level of the sub-apical actin network (Fig. 3Cb″). The GFP-CFAP206 domain, therefore, appears below the basal body in relationship to both centrin 4 and Tubg1, potentially localising to the rootlet or at the junction between the basal body and the rootlet. GFP-CFAP206 was also expressed throughout the axoneme, although at a lower level, as demonstrated by co-staining with an antibody against acetylated α-tubulin (ac. Tuba4a; Fig. 3Cc-d).

Functional analysis of *cfap206* during embryonic development of the frog *Xenopus*

The use of morpholino oligomers (MOs) to interfere with *cfap206* mRNA translation (TBMO) or splicing (SBMO) yielded variable results. Occasionally, hydrocephalus and MCC motility defects were observed, which were not consistently encountered, nor could they be rescued by co-injection of full-length murine *Cfap206* not targeted by the MOs (wild-type and GFP-fusion constructs; not shown). We therefore turned to genome editing and designed two sgRNAs targeting exon 2 and exon 5. Genome editing was confirmed via direct sequencing of PCR products with pooled DNAs from 10 F0 crispants (Fig. S3A,B). Crispant specimens were analysed for laterality defects, and nephrostome and ependymal cilia function by assessing organ situs, formation of kidney cysts and development of externally visible hydrocephalus in stage 45 tadpoles. No deviations from uninjected wild-type control specimens were observed (Fig. S4A-D).

To address potential changes in ciliary beating of *cfap206* crispants, motility of epidermal MCCs was analysed in high-speed time-lapse videos recorded from wild-type and crispant larvae at stage 32 (Movie 1). Ciliary beat frequencies were calculated as previously reported (Rachev et al., 2020) and found to be significantly elevated, from 22.5 Hz in wild type to 24.5 Hz in sgRNA1 crispants and 26.5 Hz in sgRNA2 crispants (Fig. 4Aa; Table S3). Representative kymographs illustrate these differences (Fig. 4Ab). In order to investigate whether the function of epidermal MCCs was altered in crispants, fluorescent beads were added to stage 32 larvae and bead transport was assessed in time-lapse movies (Movie 2) as described previously (Rachev et al., 2020). In comparison with wild-type specimens, bead transport was significantly reduced, from 550 µm/s in wild type to 460 µm/s in sgRNA1 crispants and 410 µm/s in sgRNA2 crispants (Fig. 4Ba; Table S2). In summary, ciliary phenotypes during embryonic frog development up to metamorphosis were restricted to the mucociliary epithelium of the larval skin, where a slight increase in ciliary beat frequency resulted in a significant reduction of cilia-mediated bead transport.

Cfap206 knockout mice suffer from hydrocephalus, defective mucociliary clearance of the airways and male infertility

To analyse the function of CFAP206 in mice, we generated a conditional allele by flanking exon 4 by loxP sites (Fig. 5A). Deletion of exon 4 by Cre-mediated site-specific recombination

Development (2020) 147, dev188052. doi:10.1242/dev.188052

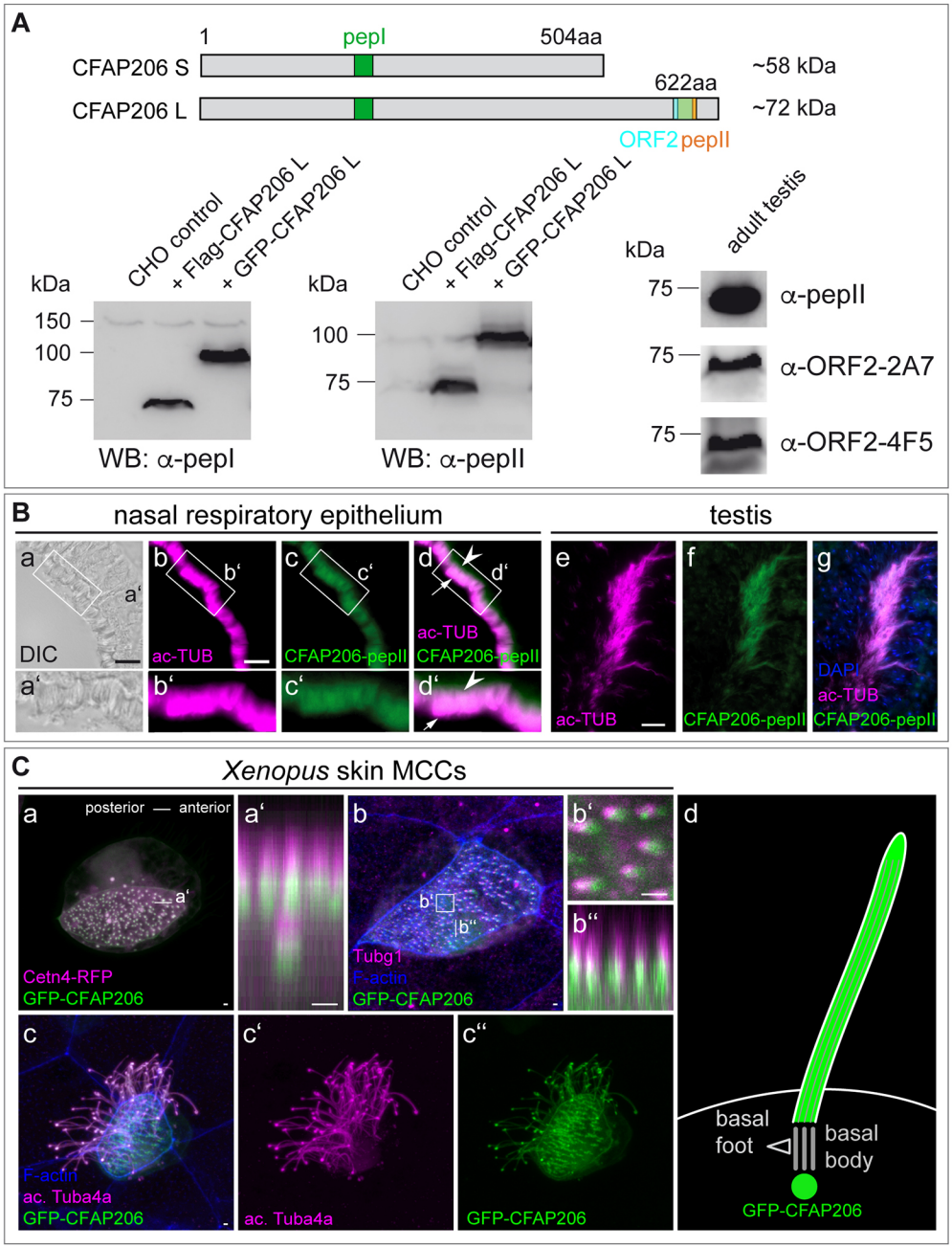

Fig. 3. Subcellular localisation of CFAP206 protein to the axoneme and basal bodies. (A) Schematic depiction of short (CFAP206S; upper row) and long (CFAP206L; lower row) CFAP206 protein. Coloured boxes indicate position of peptides (green, pepI; orange, pepII; cyan, ORF2) used to generate antibodies. Detection of tagged CFAP206 overexpressed in CHO cells and of endogenous CFAP206 protein in lysates of mouse testis with the different antibodies. The full-size western blots are shown in Fig. S9. (B) Localisation of endogenous CFAP206 (anti-pepII) to cilia on respiratory epithelial cells (a-d) and flagella of spermatozoa (e-g). Boxed areas in a-d indicate the region shown in a′-d′. Arrowheads in d and d′ indicate localisation of CFAP206 non-overlapping with acetylated α-tubulin (ac-TUB). Arrows highlight ciliary tips, which lack CFAP206. (C) Subcellular localisation of murine GFP-CFAP206 in *Xenopus* skin MCCs. (a) Co-staining with the basal body marker centrin4-RFP (Cetn4-RFP; a). Orthogonal projection shown in a′ demonstrates partial overlap at the basal body. (b) Co-staining with phalloidin to highlight F-actin and the basal foot marker tubulin gamma-1 (Tubg1) confirmed basal body staining (b′) and partial overlap at the basal foot (b″). (c-c″) Axonemal staining, as shown by co-staining with an antibody against acetylated alpha-tubulin (ac-Tuba4a). (d) Cartoon of GFP-CFAP206 localisation at the *Xenopus* cilium. Scale bars: 10 µm in B; 1 µm in C.

leads to a frame shift after amino acid 64, resulting in a stop codon 30 bp downstream in exon 5, which should prevent translation of a functional protein. To delete CFAP206 in all tissues, we excised exon 4 (*Cfap206*$^{\Delta ex4}$) in the female germ line using ZP3:Cre mice (de Vries et al., 2000). Homozygous *Cfap206*$^{\Delta ex4}$ mice were born at Mendelian ratio (wild type 147, het 306, hom 118; χ^2=5.89, *P*=0.0526) and initially showed no obvious gross abnormalities. Western blot analyses with polyclonal antibodies α-pepI and α-pepII did not reveal any CFAP206 specific signal in *Cfap206*$^{\Delta ex4/\Delta ex4}$ testis lysates (arrows in Fig. 5B), demonstrating that both CFAP206 protein variants were present in wild type and deleted in *Cfap206*$^{\Delta ex4/\Delta ex4}$ testes. Likewise, the α-pepII antibody did not detect CFAP206 protein in sections of the mutant testis and the respiratory epithelium (Fig. 5Ci,l). These data indicate that deletion of exon 4 effectively abolished translation of CFAP206 protein, i.e. that *Cfap206*$^{\Delta ex4}$ very likely represented a bona fide null allele deleting both protein variants. Therefore, the description of CFAP206 function below refers to the function of both protein variants.

Beginning 2-3 weeks after birth, 79% (118/150) of homozygous *Cfap206*$^{\Delta ex4}$ mice developed externally visible enlarged cranial vaults, suggesting ventricular dilatation and hydrocephalus (Fig. 6Ab). Dissected brains of *Cfap206*$^{\Delta ex4}$ mutants showed severely dilated and fused lateral ventricles (Fig. 6Ad). Dilated ventricles were already observed in homozygous mutants without external signs of hydrocephalus on postnatal day P1 (*n*=3/3) and P6 (*n*=4/4) (Fig. 6B). Hematoxylin-Eosin (HE) staining of mid-sagittal brain sections of P6 mutant brains revealed stenotic or closed sylvian aqueducts, which connect the 3rd to the 4th ventricle (Fig. 6C). In high-speed microscopy of P7 lateral ventricle explants, we did not detect a reduction in ependymal cilia generated flow (CGF, Fig. 6D; Movie 3; Table S5). The stenotic or closed sylvian

Development (2020) 147, dev188052. doi:10.1242/dev.188052

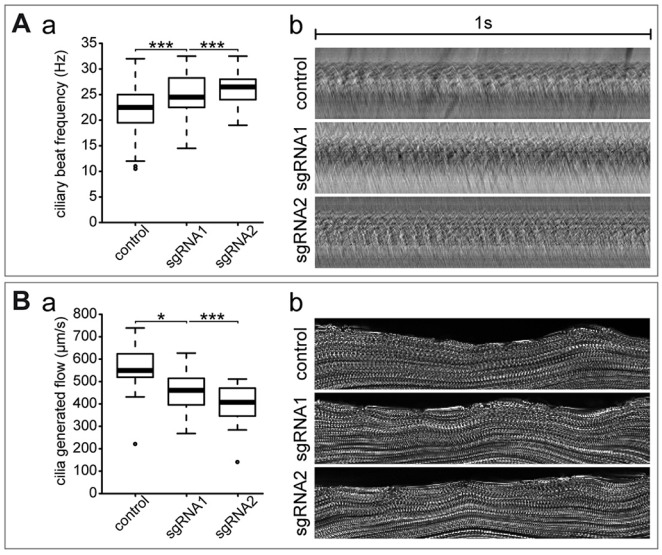

Fig. 4. Ciliary defects in MCCs of *Xenopus cfap206* crispants. (A) Enhanced ciliary beat frequency (CBF) in crispants. (a) Statistical evaluation of CBF in wild-type and *cfap206* crispants. Results from three independent experiments with 15 embryos each and five analysed MCCs per embryo. Raw data are shown in Table S3. (b) Kymographs of ciliary motility of single MCCs, generated from control wild-type, sgRNA1- and sgRNA2-injected specimens. (B) Reduced bead transport in *cfap206* crispant skin mucociliary epithelia. (a) Velocities of bead transport in wild-type, sgRNA1- and sgRNA2-injected specimens. Results from three independent experiments with eight analysed specimens each. Raw data are shown in Table S2. (b) Maximum intensity projections of single control wild-type, sgRNA1- and sgRNA2-injected embryos. The boxplots show values between the first and third quartile (boxes), with the whiskers displaying ± 1.5× the interquartile range (IQR); i.e. box length=IQR=Q3×Q1; upper whisker=Q3+1.5×IQR, lower whisker=Q1×1.5×IQR. **P*<0.05; ****P*<0.001.

aqueduct therefore appears to develop despite the establishment of postnatal flow. We further analysed whether CFAP206 might be important for the function of motile cilia in other contexts. In PAS staining of nasal cavities, we noticed mucus accumulation in mutants at different ages (3 weeks, *n*=2/3; 2 months *n*=2/2 and 8/9 months *n*=3/4; Fig. 6E). Isolated mTECs from 3- to 4-month-old wild type and *Cfap206*$^{\Delta ex4}$ mutants did not show obvious differences in cilia presence and length (Fig. 5D; Table S4). However, high-speed video analysis of ciliary beat frequency (CBF) of tracheal explant MCCs from 10 weeks up to 3-month-old animals exhibited a significant increase in CBF from an average of 12.6 Hz in wild type to about 17.3 Hz in *Cfap206*$^{\Delta ex4}$ mutants (Fig. 6Fa,b; Movie 4; Fig. S11; Table S6). The analysis of bead velocity, however, revealed no significant alterations of CGF in mutants compared with wild type in this assay (Fig. 6Fc; Movie 5; Fig. S11; Table S7), and changes of the waveform could not be assessed.

No defects in the establishment of the left-right asymmetry were observed in *Cfap206*$^{\Delta ex4/\Delta ex4}$ mutant animals (*n*=150), although *Cfap206* expression was prominent in the ventral node (Fig. 1Ea). This finding indicated that CFAP206 was dispensable for the rotational movement of cilia at the LRO. Homozygous females that did not develop hydrocephalus were fertile and raised litters normally. In contrast, homozygous males (without hydrocephalus; *n*=5) did not give rise to offspring even after prolonged matings to wild-type females. Analyses of HE-stained testis and epididymis sections showed no obvious morphological differences. The structures of seminiferous tubules and lumina-containing sperm were unaltered in mutants (Fig. 7A). Sperm quality of *Cfap206*$^{\Delta ex4}$ mutants was addressed by computer-assisted sperm analysis (CASA). Sperm cell concentration of 2- to 3-month-old mutants was similar to wild type (Fig. 7Ba; Table S8). However, the motility of mutant sperm cells was significantly reduced compared with wild type (Fig. 7Bb; Table S8). This defect was also observed by video microscopy of isolated sperm (Movie 6). Mutant sperm were unable to move effectively; motion appeared rolling or tumbling, with mutant sperm cells not moving across greater distances. In IVF (*in vitro* fertilisation) experiments, 57.8±2.8% of eggs (*n*=656/1132; three experiments; Table S9) in contact with wild-type sperm initiated embryonic development. In contrast, hardly any (0.7±0.7%; *n*=11/1657; three experiments; Table S9) eggs incubated with *Cfap206*$^{\Delta ex4/\Delta ex4}$ sperm developed into blastocysts (Fig. 7Bc; Table S9). *Cfap206*$^{\Delta ex4/\Delta ex4}$ sperm did not efficiently move towards and attach to the eggs (Fig. 7Bd,e; Movie 7), indicating that even when brought into close proximity, sperm lacking CFAP206 were unable to effectively fertilise wild-type eggs.

Sperm isolated from cauda epididymis had long flagella containing microtubules, as indicated by staining for ac-TUB (Fig. 7Cg′-i′,l′). The size and shape of nuclei (DAPI staining) and acrosomes (stained by PNA lectin) were indistinguishable from wild-type sperm (Fig. 7Cg′-l′). Staining of the fibrous sheath (by AKAP3), mitochondria (by COXIV) and annulus (by SEPTIN7) revealed the presence of distinct mid- and principal pieces (Fig. 7Ch′-l′). However, only 55% (626/1170) of mutant sperm had an extended flagellum, compared with 85.8% (1102/1274) of wild-type sperm. 40.5% (496/1170) of mutant flagella displayed a sharp bend (wild type 12.5%) and 4.6% (48/1170) were coiled (wild type 1.6%) (Fig. S5A; Table S10). Structural abnormalities were not detected by immunofluorescence staining using common markers. However, transmission electron microscopy of epididymis sections revealed highly abnormal axonemal structures. Circular (Fig. 8Ad) and bent (Fig. 8Ae) flagella were observed, which most likely represented spermatozoa shown in Fig. 7Cg,g′ and k,k′, respectively. We rarely observed normal microtubule doublets (green arrows in inset of Fig. 8Af). Most flagellar cross-sections contained variable numbers of irregularly arranged single microtubules at different flagellar levels (Fig. 8Af,f′,g,h). Groups of axonemal profiles (white asterisks in Fig. 8Af) that were surrounded by a common plasma membrane (dark blue arrows in Fig. 8Af′) were also observed. Therefore, coiled flagella found in sperm isolated from the cauda epididymis, at least in part, reflected bundles of axonemes within a common plasma membrane rather than folded or clustered flagella. The vesicular material next to the axonemal profiles (red asterisks in Fig. 8Ad,e,f′) were indicative of Golgi remnants, which might explain the structure detected in coiled flagella using the acrosomal marker PNA lectin (arrowhead in Fig. 7Cg′). Electron tomography on cryo-conserved sperm flagella from cauda epididymides revealed defects in the repetitive pattern of radial spokes (RS; Fig. 8B; Fig. S5). In wild-type sperm, RS1, RS2 and RS3 were arranged in 96 nm repeats (Fig. 8Ba; Fig. S5B). Mutants displayed one RS per 96 nm repeat (Fig. 8Bc; Fig. S5B) and an absent or incomplete RS in between, indicating that CFAP206 was needed for the establishment of radial spokes in mammalian sperm flagella.

DISCUSSION

We identified *Cfap206* in a screen for genes that act downstream of FOXJ1. Consistent with its direct or indirect regulation by FOXJ1, *Cfap206* expression correlated very well with expression of *Foxj1*, both in *Xenopus* and mouse. Ectopic *foxj1* expression in frog embryos induced *cfap206* transcription, and loss of FOXJ1 in mouse and frog embryos led to severe downregulation of *Cfap206*

Development (2020) 147, dev188052. doi:10.1242/dev.188052

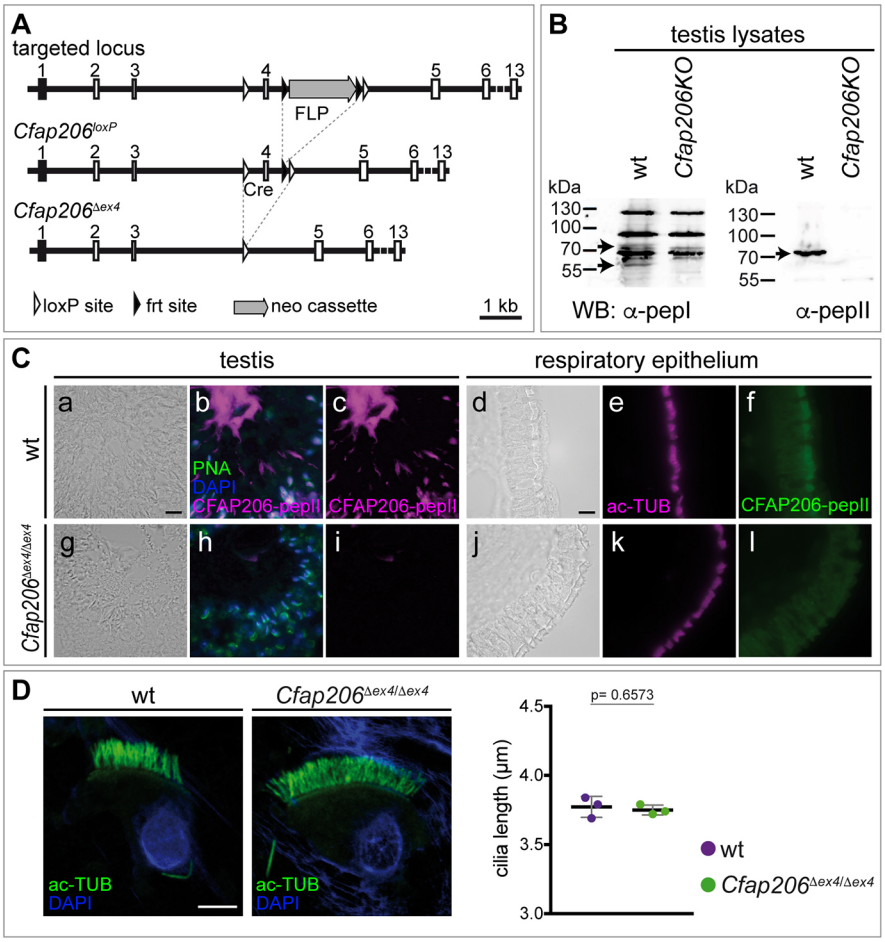

Fig. 5. Generation and characterisation of a *Cfap206*-null mouse. (A) Schematic drawing depicting the structure of the targeted locus, the locus after FLP-mediated removal of the neo cassette (*Cfap206*^{loxP}) and following Cre-mediated excision of exon 4 (*Cfap206*^{Δex4}). (B) Western blot analysis of testis lysates of wild-type and *Cfap206*$^{Δex4/Δex4}$ mice with anti-pepI and anti-pepII antibodies demonstrated absence of both CFAP206 protein variants in mutant tissue. Arrows indicate the expected sizes of the CFAP206 proteins. The full-size western blots are shown in Fig. S10. (C) Indirect immunofluorescence staining of wild-type (a-f) and *Cfap206*$^{Δex4/Δex4}$ (g-l) testis (a-c,g-i) and respiratory epithelium (d-f,j-l) sections for CFAP206, indicating loss of staining in mutant tissues. (D) Analysis of cilia length in mouse tracheal epithelial cells (mTECs) isolated from wild-type and *Cfap206*$^{Δex4/Δex4}$ mutants revealed no change in ciliary length upon CFAP206 loss. Each dot represents the average cilia length of one specimen analysed (n=3). Graph in D displays respective values as mean±s.d. Raw data are shown in Table S4. Scale bars: 10 µm in C; 5 µm in D.

mRNA expression. Here, we show that the evolutionarily conserved CFAP206 protein is essential for sperm motility in mice and modulates ciliary beat frequency of MCCs both in the *Xenopus* larva and mouse trachea. Ciliary defects during embryogenesis in *Xenopus* were restricted to the mucociliary epithelium of the larval skin, which was unexpected given the co-expression with *foxj1* from the earliest developmental stages onwards (Fig. 2). Several possible mechanisms could underlie these differences. Phenotypes may only become evident at later stages, during metamorphosis or in adult frogs. The observed mouse defects revealed themselves postnatally, in line with this reasoning. The long generation time and legal restriction to raise adult frogs prevented us from analysing this possibility. As another option, in a laboratory setting lacking environmental challenges such as poor water quality or the presence of pathogens and pollutants, *Cfap206* function may not reveal itself, particularly in the mucociliary epithelium of the larval skin, which serves as a first line of defence in much the same way as the mouse airway epithelium (Dubaissi and Papalopulu, 2011; Hayes et al., 2007; Walentek and Quigley, 2017). Loss of *cfap206* gene function may also be compensated for by upregulation of related genes (El-Brolosy et al., 2019; Rossi et al., 2015). Ciliary phenotypes in morphants, including cysts and hydrocephalus, seem to support such reasoning; however, we were unable to successfully rescue these phenotypes and prove MO specificity, which is why we did not include these datasets in our analysis. The maintenance of *cfap206* transcripts in crispant specimens (not shown) also argues against this possibility, as nonsense-mediated mRNA decay has been shown in several cases to be a prerequisite for compensation in zebrafish (El-Brolosy et al., 2019), which might be a cell type-specific phenomenon in mice (Hall et al., 2013). Short of a biochemical understanding of Cfap206 function, we cannot discriminate between these and other possible explanations at this time.

In mouse, *Cfap206* gives rise to two transcripts that were detected in all analysed tissues and cell lines. Whether both transcripts (and the resulting protein variants) are present in the same cell remains to be determined. As CFAP206L was detected in apparently all cilia of respiratory MCCs (e.g. Fig. 3B), and both transcripts were present in this tissue, it is reasonable to assume that both proteins co-exist in cells carrying motile cilia, the functional significance of which is unknown thus far. CFAP206L is more similar in length to FAP206 from *Tetrahymena* (622 versus 635 amino acids), which might indicate that this protein is the fully functional variant. To analyse whether CFAP206 S is sufficient to substitute for CFAP206L will require the generation of a mutant allele that specifically removes CFAP206L. Notwithstanding potential functional differences of these two protein variants, our null allele should delete all CFAP206 functions, because both protein variants were effectively eliminated.

In *Tetrahymena*, FAP206 acts as a microtubule-docking adapter for RS2 (Vasudevan et al., 2015). The knockout of FAP206 in *Tetrahymena* resulted in the loss of RS2, in some cases absence of RS3 as well, leading to an abnormal flagellar waveform and a reduction of the swim rate to 30% (Vasudevan et al., 2015). This function appears to be conserved in mouse sperm cells, as one or two RSs were missing in mutants (Fig. 8B; Fig. S5B,C). The resolution of our tomography does not allow to unequivocally

Development (2020) 147, dev188052. doi:10.1242/dev.188052

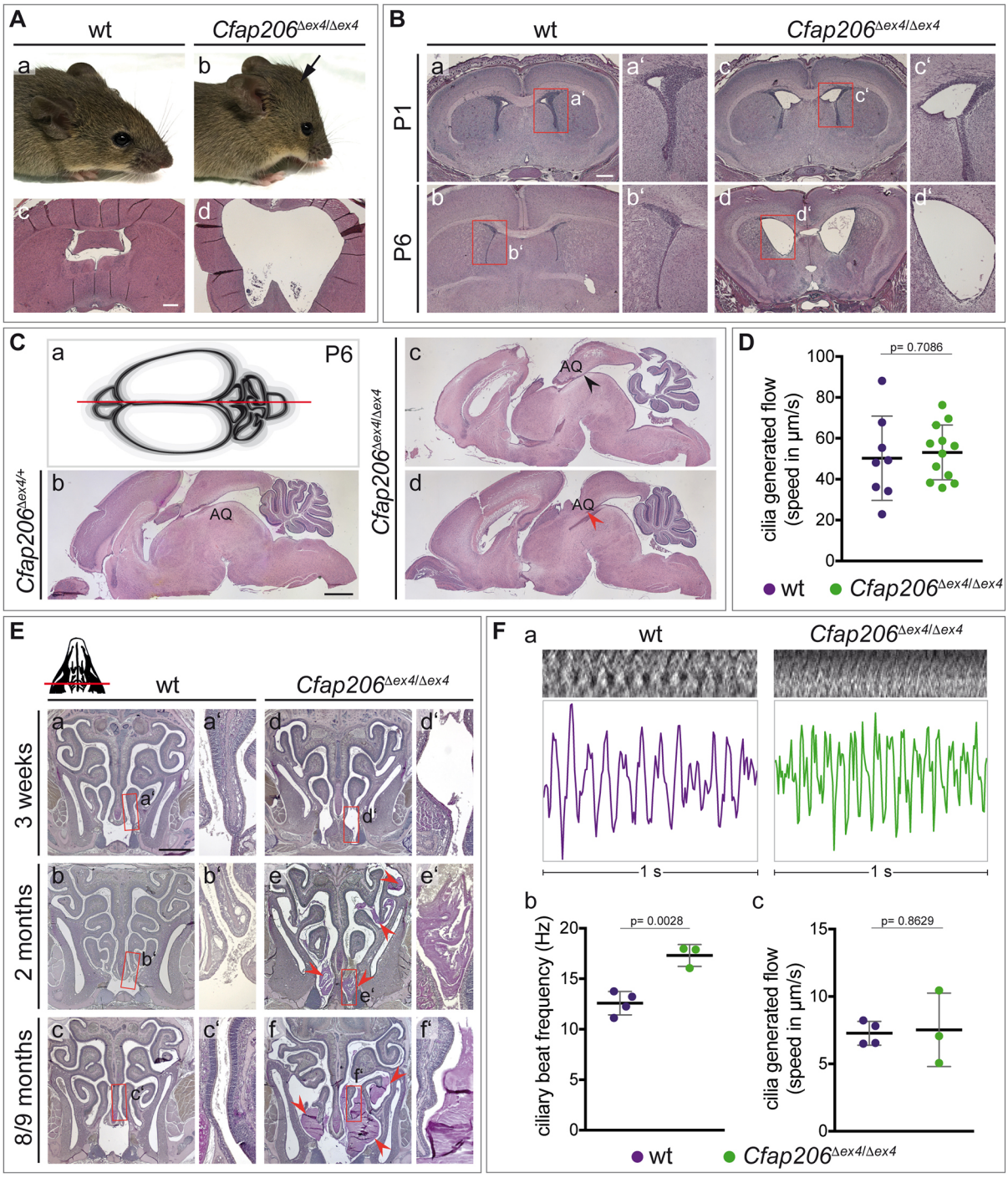

Fig. 6. Enlarged ventricles and mucus accumulation in *Cfap206*$^{\Delta ex4/\Delta ex4}$. (A) External views (a,b) and Hematoxylin and Eosin-stained coronal sections (c,d) of wild-type (a,c) and *Cfap206*$^{\Delta ex4/\Delta ex4}$ (b,d) heads revealed domed skull, and expanded and fused ventricles of *Cfap206*$^{\Delta ex4/\Delta ex4}$ mutants. (B) Hematoxylin and Eosin-stained coronal sections of wild-type (a-b′) and *Cfap206*$^{\Delta ex4/\Delta ex4}$ mutant (c-d′) brains demonstrated the presence of enlarged ventricles on postnatal day 1 (P1). Boxed areas in a-d indicate the regions shown at higher magnification in a′-d′. (C) (a) Schematic representation of a P6 brain. Red line indicates plane of section. The mid-sagittal sections of heterozygous *Cfap206*$^{\Delta ex4}$ (representing wild-type condition; b) and homozygous *Cfap206*$^{\Delta ex4}$ mutants (c,d) were Hematoxylin and Eosin stained to visualise the aqueduct (AQ). Homozygous mutants showed stenotic (black arrowhead in c) or obstructed (red arrowhead in d) aqueducts. (D) Cilia-generated ventricular flow at P7 was comparable in wild-type and *Cfap206*$^{\Delta ex4/\Delta ex4}$ littermates. Each dot represents the average speed of all tracked particles of a single individual (wild type n=8 and *Cfap206*$^{\Delta ex4/\Delta ex4}$ n=12). Numerical values used to generate the dot plot are shown in Table S5. (E) Coronal sections of wild-type (a-c′) and *Cfap206*$^{\Delta ex4/\Delta ex4}$ mutant (d-f′) nasal cavities, demonstrating progressive mucus accumulation in mutants. Boxed areas in a-f indicate regions shown at higher magnification in a′-f′. (F) Kymographs and derived CBF. (a) Representative kymographs (upper panels) and plotted values (lower panels) of wild-type (violet) and *Cfap206*$^{\Delta ex4/\Delta ex4}$ (green) tracheal cilia motility (t=1 s) depict ciliary beat frequency (CBF). (b) CBF of cilia of *Cfap206*$^{\Delta ex4/\Delta ex4}$ tracheas was enhanced compared with wild type. Each dot represents the average CBF of one specimen analysed (wild type, n=4; *Cfap206*$^{\Delta ex4/\Delta ex4}$, n=3). Additional details of CBF measurements are shown in Fig. S11. Raw data are shown in Table S6. (c) Cilia-generated flow (CGF) was unchanged in *Cfap206*$^{\Delta ex4/\Delta ex4}$ trachea explants compared with wild type. Raw data are shown in Table S7. Data are mean±s.d. Individual dots represent individual data points. Scale bars: 500 µm in Ac,d,B; 1 mm in C,E.

Development (2020) 147, dev188052. doi:10.1242/dev.188052

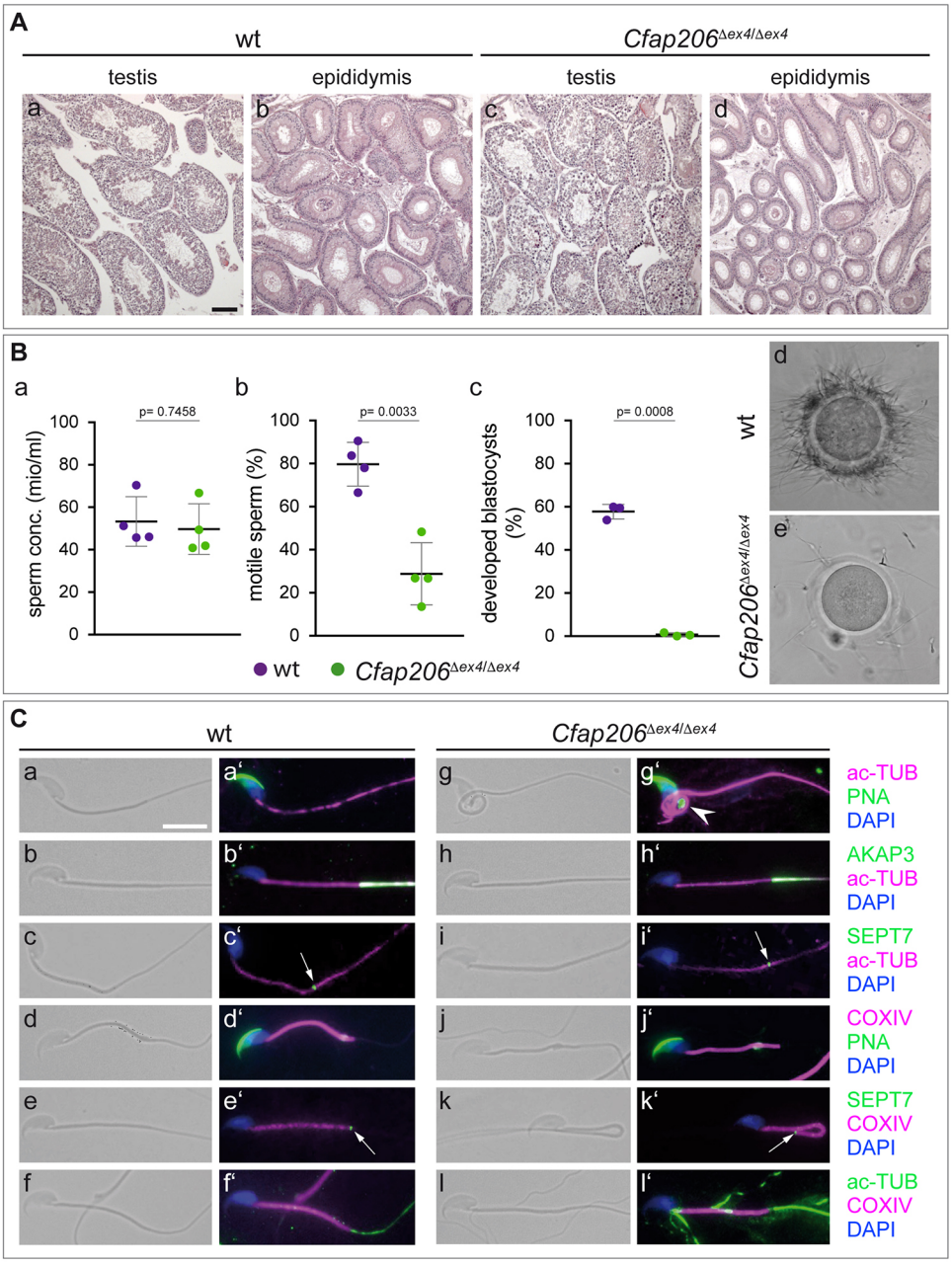

Fig. 7. Non-functional spermatozoa of *Cfap206*$^{\Delta ex4/\Delta ex4}$ mutant males. (A) Hematoxylin and Eosin-stained sections of wild-type (a,b) and *Cfap206*$^{\Delta ex4/\Delta ex4}$ mutant (c,d) testes (a,c) and epididymides (b,d). (B) CASA analysis and results of IVF showing normal sperm concentration in *Cfap206*$^{\Delta ex4/\Delta ex4}$ mutants (a), reduced *Cfap206*$^{\Delta ex4/\Delta ex4}$ sperm motility (b), inability of *Cfap206*$^{\Delta ex4/\Delta ex4}$ sperm to support early development after IVF (c) and reduced attachment to the zona pellucida *in vitro* (e). (d) Wild-type egg with wild-type sperm cells. (e) Wild-type egg with *Cfap206*$^{\Delta ex4/\Delta ex4}$ sperm. Raw data from CASA analysis (a,b) and IVF (c) are shown in Table S8 and Table S9, respectively. (C) Bright-field (a-l) and fluorescence (a′-l′) images of wild-type (a,a′-f,f′) and *Cfap206*$^{\Delta ex4/\Delta ex4}$ (g,g′-l,l′) sperm cells isolated from the cauda epididymis. The following dyes and antibodies were used to visualise organelles and subcellular compartments: DAPI (nuclei; a′-l′; blue); anti-ac-TUB (axonemes; a′-c′,g′-i′; magenta); PNA-lectin (acrosomes; a′,g′,h′,j′; green); anti-AKAP3 (fibrous sheath; b′,h′; green); anti-SEPT7 (annuli; c′,e′,i′,k′; green); and anti-COXIV (mitochondria; d′-f′,j′-l′; magenta). Arrowhead in g′ highlights a coiled flagellum with PNA-stained material; arrows in c′,e′,i′,k′ indicate annuli. Data are mean±s.d. in B with individual data points shown. Scale bars: 100 µm in A; 10 µm in C.

identify the consistently present radial spoke as RS1. However, given the specific function as an adapter for RS2 in *Tetrahymena*, it seems reasonable to assume that the RS consistently observed at 96 nm distance in mutant mouse sperm is RS1. A RS-related function of CFAP206 is also supported by its absence from the ciliary tip that apparently lacks radial spokes (reviewed by Osinka et al., 2019; Reynolds et al., 2018; Soares et al., 2019) and would be consistent with the lack of laterality defects in mouse and frog, as motile cilia at the LRO lack the central pair and RSs and show a rotational movement (Nonaka et al., 1998). The absence of LR defects is also a characteristic of individuals with PCD with defects in radial spokes and the central pair (Edelbusch et al., 2017; Lucas et al., 2019).

Loss of RS2 in *Tetrahymena* FAP206 mutants caused compressed ciliary cross-sections but did not disrupt the central pair or outer microtubule doublets (Vasudevan et al., 2015). Disruption of RS assembly in mouse ependymal cells by depletion of RSPH9 abolished the central pair but left the outer doublets largely intact (Zhu et al., 2019). RS deficiency in *Chlamydomonas* resulted in a lateral shift of the central pair, without impact on the outer doublets (Sivadas et al., 2012). This contrasts with defective microtubular doublets that we frequently observed in mouse sperm flagella, suggesting that CFAP206 has additional microtubule-stabilising functions in the specialised cilium of mammalian sperm. The identification of these functions should be aided by the identification of CFAP206-interacting proteins in sperm cells. With this aim in mind, we identified potential interaction partners by immunoprecipitation of CFAP206 from adult mouse testes and subsequent mass spectrometry. These analyses led to a number of promising candidate proteins (Table S11) that – following validation – should provide further insights into CFAP206 function.

In contrast to the largely immotile sperm cell flagella, cilia on multiciliated tracheal cells were motile and even showed an

Development (2020) 147, dev188052. doi:10.1242/dev.188052

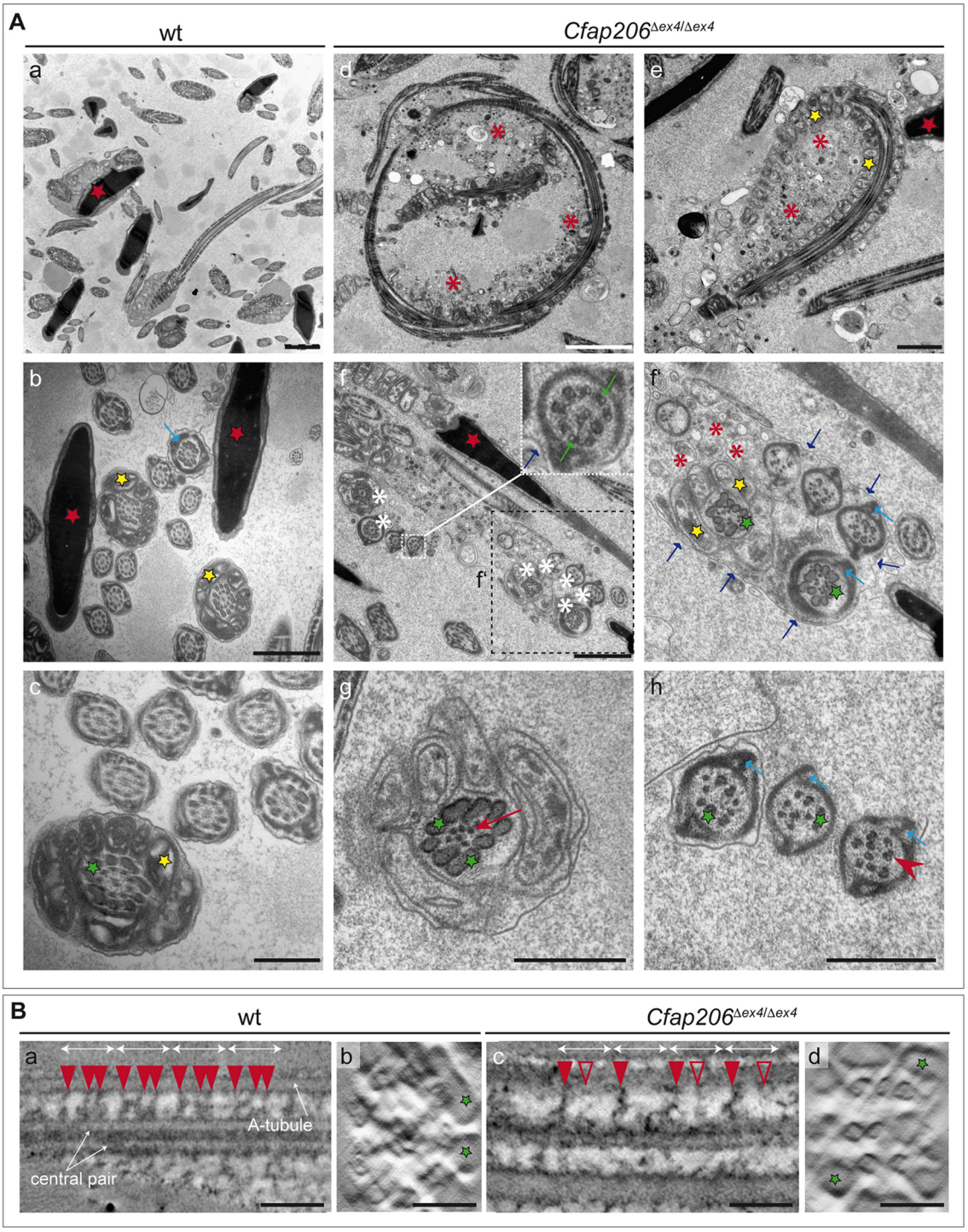

Fig. 8. Electron microscopic analysis of wild-type and *Cfap206*$^{\Delta ex4/\Delta ex4}$ mutant sperm. (A) TEM analysis of wild-type (a-c) and *Cfap206*$^{\Delta ex4/\Delta ex4}$ (d-h) epididymis sperm. (a-c) Overviews of wild-type sections; red stars, sperm heads; blue arrow, fibrous sheath; yellow star, mitochondria; green stars, ODFs. (d,e) Longitudinal section through *Cfap206*$^{\Delta ex4/\Delta ex4}$ circular (d) or bent (e) axonemes surrounding vesicular material (red asterisks). (f) Groups of axonemes (marked with white asterisks) surrounded by a single plasma membrane (dark-blue arrows in f′, magnified region of the black outlined area in f) and axonemal profiles with apparently normal microtubule doublets (green arrows in white outlined inset). (f′) Vesicular structures (red asterisks) and multiple axonemal profiles from the midpiece and principal piece region [indicated by the presence of mitochondria (yellow stars) and fibrous sheath (light-blue arrows)] with disorganized microtubules and ODFs (green stars) surrounded by a single plasma membrane (dark-blue arrows). (g) Axonemal profile of the midpiece region showing few irregular single microtubules (red arrow) and ODFs (green stars). (h) Axonemal profiles of principal pieces with disorganized ODFs (green stars) and microtubules surrounded by fibrous sheaths (light-blue arrows). (B) Electron tomography revealed radial spokes (red arrowheads) between the inner central pair of microtubules and the outer microtubules (anchored at the A-tubule) in wild type (a). Radial spokes (red arrowheads, RS1-3) appeared in a repetitive pattern, interrupted by electron lucent gaps repeating every 96 nm. In *Cfap206*$^{\Delta ex4/\Delta ex4}$ mutant sperm tails (c), the radial spokes were rather irregular and/or incomplete (unfilled red arrowheads) and missing. (b,d) Cross-sections of the wild-type and *Cfap206*$^{\Delta ex4/\Delta ex4}$ tomograms shown in a,c, respectively. Green stars indicate ODFs. Further details of the tomography and section planes are shown in Fig. S5B,C. Scale bars: 2 µm in Aa,d; 1 µm in Ab,e,f; 500 nm in Ac,g,h; 100 nm in B.

Development (2020) 147, dev188052. doi:10.1242/dev.188052

enhanced beating frequency. Although we cannot exclude the possibility of subtle deviations in the ciliary beating patterns, the motility of these cilia suggests that they do not have major structural defects. In line with this notion, individuals with PCD with defects in RS function show very subtle ciliary beating abnormalities, and cross-sections of respiratory cilia can reveal normal ultrastructure (Burgoyne et al., 2014; Castleman et al., 2009; e.g. Frommer et al., 2015; Knowles et al., 2014; Ziętkiewicz et al., 2012). The increased beating frequency of *Cfap206* mutant cilia was accompanied by a reduction of the speed of cilia-generated flow to about 80% in the frog larval skin (Movies 1, 2 and Fig. 4), but had no apparent effect on the speed of cilia-generated flow in mouse tracheal explants (Fig. 6F). This differs from *Tll1* (Ikegami et al., 2010) and *Cfap43* mutants (Rachev et al., 2020), in which an increase in beating frequency was associated with reduced cilia-generated flow. Although loss of CFAP206 clearly affects ciliary beating in respiratory epithelium, it remains to be seen how this relates to mucous accumulation. It appears plausible, however, that mucous accumulation is causatively linked to the altered ciliary beat frequency. Altered frequencies may result in subtle alterations of the ciliary wave form and/or changes of beating asymmetry, which might reduce efficient flow in the native lung and lead to mucus accumulation over time.

Similar to flow generated by MCCs of the trachea, ependymal flow in explants of postnatal lateral ventricles (P7) was apparently unaltered, although enlarged ventricles were present accompanied by obstruction of the aqueduct (Fig. 6C). It is unclear whether apparently normal flow is maintained in older animals (which could not be analysed due to restrictions by animal welfare regulations). Aqueduct obstruction, maintenance of flow generated by ependymal cells of the lateral walls of the lateral ventricle and build-up of pressure might all contribute to the highly penetrant progression of ventricle enlargement after P14. The basis for the development of hydrocephalus in *Cfap206* mutants already at P1, prior to the presence of motile cilia on the lateral ventricular walls (Banizs et al., 2005) and the onset of postnatal flow, is less clear. It suggests that CFAP206 function is required early on, during embryonic development. Consistent with this notion, *Cfap206* was already detected at E16.5 in the developing brain, although at low levels (Fig. S6). Analyses of *Ccdc39* mutant mice revealed that ependymal MCCs with motile cilia are present on the ventro-medial wall of the lateral ventricle around P1. Functional impairment of these motile cilia led to enlarged ventricles shortly after birth (Abdelhamed et al., 2018), prior to the emergence of motile cilia on the lateral ventricular walls (Banizs et al., 2005) and the onset of postnatal flow. Loss of CFAP206 might therefore impact on early flow and lead to early aqueduct obstruction, which blocks drainage of cerebrospinal fluid causing subsequent progressive lateral ventricle enlargement. A requirement of ependymal flow to keep the aqueduct postnatally open has been established in *Mdnah5* mutant mice. These lacked directed ependymal flow at lateral ventricles and developed hydrocephalus beginning at P6, with subsequent stenosis of the aqueduct at P12, which was attributed to the absence of postnatal ependymal flow (Ibañez-Tallon et al., 2004).

In conclusion, our descriptive and functional analysis of *Cfap206* in mouse and *Xenopus* demonstrated that this highly conserved ciliary gene functions in defined ciliary contexts, predominantly at post-embryonic stages in both species. Male sterility caused by severe flagellar malformations in mice suggests that mutations of CFAP206 may also underlie male infertility in humans. Mutant alleles might lead to milder forms of PCD, without clear ultrastructure cilia defects and only subtle changes of ciliary movement, which might complicate diagnosis of patients.

MATERIALS AND METHODS

Ethics statement and husbandry of mice and frogs

Mice and *Xenopus laevis* were handled in accordance with the German laws and regulations (Tierschutzgesetz). All procedures were approved by the ethics committee of Lower Saxony for care and use of laboratory animals LAVES and by the Regional Council Stuttgart, Germany (A379/12 Zo, 'Molekulare Embryologie', V340/17 ZO and V349/18 ZO, '*Xenopus* Embryonen in der Forschung'). *Xenopus* embryos obtained by *in vitro* fertilisation were maintained in 0.1× modified Barth medium (Sive et al., 2000) and staged according to Nieuwkoop and Faber (1994).

Mice were housed in the animal facility of Hannover Medical School (ZTL) as approved by the responsible Veterinary Officer of the City of Hannover, Germany. Animal welfare was supervised and approved by the Institutional Animal Welfare Officer.

Multiple sequence alignment of CFAP206 proteins

Sequences were aligned using ClustalW (v1.83; multiple sequence alignment; Pairwise Alignment Mode: Slow; Pairwise Alignment Parameters: Open Gap Penalty=10.0, Extend Gap Penalty=0.1, Similarity Matrix: gonnet; Multiple Alignment Parameters: Open Gap Penalty=10.0, Extend Gap Penalty=0.2, Delay Divergent=30%, Gap Distance=4; Similarity Matrix: gonnet).

Mouse methods

Generation of *Cfap206*$^{\Delta ex4}$ mice

Cfap206^{loxP} mice were generated by Cyagen Biosciences. The positive selection marker (neo cassette) was flanked by FRT sites and removed by FLP-mediated recombination. Germ-line deletion of exon 4 was achieved by crossing of *Cfap206*^{loxP}; ZP3:Cre (de Vries et al., 2000) double heterozygous females to wild-type males. The floxed allele was originally generated on the C57BL/6 background. Breeding to FLPe and ZP3:Cre mice generated a mixed genetic background (predominantly 129Sv/CD1), on which the strain was maintained. The phenotype of *Cfap206*$^{\Delta ex4}$ mice was analysed on this mixed genetic background. *Foxj1*$^{-/-}$ mutant mice (*Foxj1*^{lacZ}) have been described previously (Brody et al., 2000) as have FLPe mice (Rodríguez et al., 2000).

Genotyping of mice

Cfap206 mutant and wild-type mice were genotyped by PCR with allele-specific primer pairs: Cfap206-loxP-F1, 5′-ATCACGGAGTCAGGGCT-AAGTTG-3′; Cfap206-loxP-R1, 5′-GGCAAGCAGTCTACCAACTGA-GG-3′ (producing a 238 bp wild-type and a 299 bp *Cfap206*^{loxP} product); Cfap206-loxP-F1, 5′-ATCACGGAGTCAGGGCTAAGTTG-3′; Cfap206-R1, 5′-CCAACCAGCCCATACTATTC-3′ (producing a 246 bp *Cfap206Δex4* and a 1225 bp wild-type product).

Reverse transcription-PCR from total RNA

Total RNA was isolated from dissected mouse tissues using TriReagent (Zymo Research). cDNA was synthesised using SuperScriptII Reverse Transcriptase (Invitrogen), according to the manufacturer's instructions. PCR was performed using primer pairs: Cfap206_Ex8for, 5′-TCCCAAG-TCTTCCCCATCTTCG-3′; Cfap206_Ex12rev, 5′-TGTGTGTATCTGTC-TGTGTGCCG-3′ (specific for the *Cfap206* mRNA encoding the long protein, 619 bp product; shown in Fig. 1B); Cfap206_RTex9for, 5′-CGA-TGGCGTCGTCGTGAAAAG-3′; Cfap206_RTex13rev, 5′-CCCACGA-AGGCCAGCTATGAA-3′ (specific for the *Cfap206* mRNA encoding the long protein, 697 bp product; shown in Fig. S1B); Cfap206_Ex8for, 5′-AAAATCTAAGACGGCGGTCCC-3′; Cfap206_Ex11rev, 5′-AGTCA-GGAGTTACAAACCCAGGTG-3′ (specific for the *Cfap206* mRNA, encoding the short protein, 619 bp product; shown in Fig. 1B and Fig. S1B); Hprt_RT_for_ex7, 5′-GCTGGTGAAAAGGACCTCT-3′; Hprt_RT_rev_ex9, 5′-CACAGGACTAGAACACCTGC-3′ (specific for the *Hprt* mRNA, 248 bp product); Foxj1_RT_for_ex2, 5′-CTTCTGCTACTT-CCGCCATGC-3′; Foxj1_RT_rev_ex3, 5′-TCCTCCTGGGTCAGCAGTA-AGG-3′ (specific for the *Foxj1* mRNA, 432 bp product).

Tissue collection, embedding and sectioning

Mice were killed by cervical dislocation and dissected tissues were fixed at 4°C in 4% PFA or 100% methanol overnight. If necessary, materials were

Development (2020) 147, dev188052. doi:10.1242/dev.188052

decalcified in 0.5 M EDTA for several days up to 2 weeks, with EDTA changes every other day. Subsequently, the tissues were dehydrated and embedded in paraffin according to standard procedures. Embedded tissues were sectioned at 5 or 10 µm. Sperm cells were isolated as described previously (Rachev et al., 2020).

Histological methods

Histological staining was performed on 10 µm sections of PFA fixed and paraffin-embedded tissues. HE staining was performed according to standard procedures. Periodic Acid-Schiff (PAS) staining was carried out using the Sigma Aldrich PAS staining kit (395B).

Section and whole-mount *in situ* hybridisation

Section *in situ* hybridisation was performed on 10 µm paraffin sections of formaldehyde-fixed tissues that were dewaxed, hydrated, digested with Proteinase K, fixed with formaldehyde and hybridised overnight at 70°C (Moorman et al., 2001). The DIG-labelled RNA probe was synthesised from *Cfap206* cDNA (Fantom clone accession number AK005650, coordinates ZX00119D08), using the Roche DIG RNA labelling system. Whole-mount *in situ* hybridisation was carried out using standard procedures described previously (Stauber et al., 2017). Section and whole-mount *in situ* hybridisation results were documented with a Leica DM5000B microscope with Leica Firecam software.

Isolation and processing of sperm cells for video microscopy or immunofluorescence staining

For isolation of sperm cells, cauda epididymis was collected and cut into 2-3 mm pieces that were transferred into HTF medium (101.65 mM NaCl, 4.7 mM KCl, 199.5 µM $MgSO_4$, 370.5 µM KH_2PO_4, 25 mM $NaHCO_3$, 2.7 mM $CaCl_2$, 2.8 mM glucose, 0.33 mM sodium pyruvate, 18.3 mM sodium lactate, pen/strep, 0.0002% Phenol Red and 4 mg/ml BSA). The dissected epididymis was agitated for 15 min at 600 rpm. For video microscopy, sperm was incubated in HTF containing 0.5% methyl-cellulose for 1 h before documentation. PBS containing sperm was spread on glass slides and dried before further processing.

Computer assisted sperm analysis (CASA)

Sperm cells were isolated from the cauda epididymis in 150 µl HTF medium and capacitated for 90 min at 37°C. Aliquots of 3 µl sperm suspension were analysed in a Leja Standard Count 4 Chamber Slide using an Olympus CX41 (Zuber Optik) and the QualiSperm software (Biophos optimised for human sperm), which measures motility rates and concentration of sperm. Statistical analysis was performed with Prism (GraphPad) using a two-tailed *t*-test.

In vitro fertilisation (IVF)

Sperm cells isolated from the cauda epididymis were capacitated for 2 h at 37°C in 5% CO_2 and 5% O_2 in HTF medium. Eggs were isolated from wild-type females, incubated in HTF in groups of 40 with sperm for 6 h at 37°C under oil, washed in HTF and after 24 h transferred to KSOM medium. Development of embryos was tracked until day 7.5 after IVF. Statistical analysis was performed with Prism (GraphPad) using two-tailed *t*-test.

Cell culture

CHO, mIMCD3 and L-cells were maintained in DMEM/F12 (Gibco) containing 10% FCS, pen/strep and 2 mM Glutamax. Transfections of CHO cells were performed using Perfectin (Genlantis) according to manufacturer's instructions.

Generation of CFAP206 specific antibody

Rabbit polyclonal antibodies detecting CFAP206 were produced by immunisation of rabbits with mouse CFAP206 peptide IRLFNRDSGKGGEG (pepI; amino acids 194-207) and KEASTQSKREGSSR (pepII; amino acids 576-589). The antibodies were generated by Biogenes. Peptides were selected according to: hydrophilicity (according to Kyte-Doolittle); surface probability (according to Emini); chain flexibility (according to Karplus-Schulz); secondary structure (according to Chou-Fasman); and antigenicity index (according to Jameson-Wolf). CFAP206 antibodies were purified using the respective CFAP206 polypeptide and SulfoLink coupling resin (Thermo Fisher Scientific). Purification was performed according to the manufacturer's instructions.

Monoclonal antibodies (mAbs) against mouse CFAP206 epitope PLKEASTQSKREG (ORF2; amino acids 574-586) were generated as described previously (Rachev et al., 2020). mAbs that reacted specifically with CFAP206 were analysed on western blots. In this study, α-ORF2-2A7 (rat IgG2a) 1:1 and α-ORF2-4F5 (rat IgG2c) 1:1 were used.

Immunofluorescence staining

Paraffin sections were deparaffinised and rehydrated, and antigens were unmasked by boiling for 20 min in 10 mM Tris-HCl (pH 9.5) and 1 mM EDTA. Dried sperm were washed in PBS. To block unspecific binding, 5% FCS in PBS was used. Primary antibodies were incubated overnight at 4°C, secondary antibodies for 1 h at room temperature. Antibodies were diluted in blocking solution. The following primary antibodies were used: anti-acetylated α-tubulin (ac-TUB) *Clone 6-11B-1*; (axoneme; Sigma Aldrich, T6793) 1:1000, anti-gamma-Tubulin (γ-TUB) Clone GTU-88; (basal body; Sigma Aldrich, T5326) 1:4000, anti-CFAP206 (pepII) testis 1:50; nasal cavity and lung 1:10; anti-AKAP3 (fibrous sheath; Proteintech, 13907-1-AP) 1:200; anti-COXIV (mitochondria; Abcam, ab202554) 1:200; and anti-SEPTIN7 (annulus; IBL international, 18991) 1:200. The following secondary antibodies were used: anti-mouse-Alexa555 (Invitrogen, A21424) 1:500; anti-rabbit-Alexa555 (1:1000, Invitrogen, A21429); anti-mouse-Alexa488 (1:1000, Invitrogen, A11029); anti-rabbit-Alexa488 (Invitrogen, A11034) 1:500. DAPI (0.5 µg/ml, Applichem) and PNA-lectin-Alexa488 (1:250-500, Invitrogen L-21409) were incubated together with secondary antibodies.

Image processing

All images were processed and analysed using Fiji (ImageJ). Brightness and contrast were adjusted with Fiji and in immunofluorescence staining the red channels (Alexa555 detection) were changed to magenta to make images accessible to colour vision impaired readers.

Isolation of mouse tracheal epithelial cells (mTECs)

mTECs were isolated by tracheal brushing as described previously (Rachev et al., 2020).

Ex vivo imaging of mouse tracheal multiciliated cells: flow tracking and beat frequency analysis

Tracheas of 10 weeks to 3-month-old wild-type and $Cfap206^{\Delta ex4/\Delta ex4}$ mice were dissected and analysed as described previously (Rachev et al., 2020) using a method based on that described by Francis and Lo (2013).

Determination of ciliary flow in lateral ventricles

Explanted P7 mouse brains were analysed as described previously (Rachev et al., 2020).

Transmission electron microscopy (TEM)

Caudae epididymides were dissected from 3-month-old wild-type and $Cfap206^{\Delta ex4/\Delta ex4}$ littermates, fixed, embedded and analysed as described previously (Rudat et al., 2014).

Electron tomography

Epididymides of wild-type and $Cfap206^{\Delta ex4/\Delta ex4}$ males were freshly prepared and high-pressure frozen as described previously (Guzman et al., 2014). Sections (300 nm) were imaged in a Tecnai 20 operated at 200 kV. Two tilt series with 90° rotations were recorded from −60° to +60° with an increment of 1°. Tomograms were generated using imod (Kremer et al., 1996), using 10 nm gold beads as fiducials, applied to both sides of the sections. The final tomogram was displayed in the slicer window with a section plane parallel to the central pair of microtubules.

Immunoprecipitations for mass spectrometry

CFAP206 was immunoprecipitated from mouse testis (excluding epididymis) using the Pierce crosslink IP kit (Thermo Scientific) with

Development (2020) 147, dev188052. doi:10.1242/dev.188052

anti-pepII antibody. Immunoprecipitation was performed according to the manufacturer's instructions with some modifications. Lysebuffer (150 mM NaCl; 50 mM Tris-HCl, pH 7.4; 0.55% Nonidet P40; 1× Halt Prot/Phos Inhibitor Mix) and Washbuffer (150 mM NaCl; 50 mM Tris-HCl, pH 7.4; 0.12% Nonidet P40; 1× Halt Prot/Phos Inhibitor Mix) were optimised for anti-CFAP206-pepII. For elution, 60 µl Neutralisationbuffer (1 M Tris-HCl, pH 8) was added per reaction tube, and elution was carried out three times using 200 µl Elutionbuffer (200 mM glycine, pH 2.5). For mass spectrometry analysis, 10 independent wild-type and 10 independent *Cfap206*$^{\Delta ex4/\Delta ex4}$ IPs (technical replicates) were used, collected from three different animals (biological replicates).

Mass spectrometry

Eluates were precipitated with chloroform and methanol followed by trypsin digestion as described previously (Gloeckner et al., 2009). C-MS/MS analysis was performed on Ultimate3000 nanoRSLC systems (Thermo Scientific) coupled to an Orbitrap Fusion Tribrid mass spectrometer (Thermo Scientific) by a nano spray ion source. Tryptic peptide mixtures were injected automatically and loaded at a flow rate of 30 µl/min in 0.1% trifluoroacetic acid in HPLC-grade water onto a nano trap column (300 µm i.d.×5 mm Pre column, packed with Acclaim PepMap100 C18, 5 µm, 100 Å; Thermo Scientific). After 3 min, peptides were eluted and separated on the analytical column (75 µm i.d.×25 cm, Acclaim PepMap RSLC C18, 2 µm, 100 Å; Thermo Scientific) by a linear gradient from 2% to 30% of buffer B (80% acetonitrile and 0.08% formic acid in HPLC-grade water) in buffer A (2% acetonitrile and 0.1% formic acid in HPLC-grade water) at a flow rate of 300 nl/min over 117 min. Remaining peptides were eluted by a short gradient from 30% to 95% buffer B in 5 min. Analysis of the eluted peptides was carried out on an LTQ Fusion mass spectrometer. From the high-resolution MS pre-scan with a mass range of 335 to 1500, the most intense peptide ions were selected for fragment analysis in the orbitrap, using a high-speed method if they were at least doubly charged. The normalized collision energy for HCD was set to a value of 27 and the resulting fragments were detected with a resolution of 120,000. The lock mass option was activated; the background signal with a mass of 445.12003 was used as lock mass (Olsen et al., 2005). Every ion selected for fragmentation was excluded for 20 s by dynamic exclusion. MS/MS data were analysed using the MaxQuant software (version 1.6.1.0) (Cox and Mann, 2008; Cox et al., 2009). As a digesting enzyme, Trypsin/P was selected with maximal 2 missed cleavages. Cysteine carbamidomethylation was set for fixed modifications, and oxidation of methionine and N-terminal acetylation were specified as variable modifications. The data were analysed by label-free quantification with the minimum ratio count of 3. The first search peptide tolerance was set to 20, the main search peptide tolerance to 4.5 ppm and the re-quantify option was selected. For peptide and protein identification, the mouse subset of the SwissProt database (release 2014_04) was used and contaminants were detected using the MaxQuant contaminant search. A minimum peptide number of 2 and a minimum length of 7 amino acids was tolerated. Unique and razor peptides were used for quantification. The match between run option was enabled with a match time window of 0.7 min and an alignment time window of 20 min. For each genotype, eight technical replicates derived from three wild-type and three mutant males were analysed. The statistical analysis, including ratio, *t*-test and significance A calculation, was carried out using the Perseus software (version 1.5.5.3; Tyanova et al., 2016). The full mass spectrometry proteomics data have been deposited with the ProteomeXchange Consortium via the PRIDE (Vizcaíno et al., 2016) partner repository with the dataset identifier PXD018554.

Xenopus methods

Microinjections

Xenopus laevis embryos were injected at the four-cell stage into defined lineages to target neural (hydrocephalus), axial mesodermal (laterality), paraxial mesodermal (kidney) or epidermal cells. Drop size was calibrated to 4 nl per injection. Alexa Fluor 488 dextran was added as a lineage tracer (MW 70,000 or 10,000, 0.5-1 µg/µl; Thermo Fisher Scientific).

Whole-mount *in situ* hybridisation

In situ hybridisation was performed using standard procedures. Histological sections (30 µm) were prepared following embedding of embryos in a gelatine-albumin mix using a vibratome (Leica).

Statistical analysis of *Xenopus* phenotypes

FIJI was used for all measurements. χ^2 analysis was performed to calculate significances of occurrence of organ situs defects and kidney cyst.

CRISPR/Cas9-mediated genome editing

The CRISPRscan algorithm was used to design single guide RNAs (sgRNAs; Moreno-Mateos et al., 2015). sgRNAs targeting exon 2 and 5 were transcribed using the MEGAshortscript T7 Kit (Invitrogen) from synthetic DNA oligomers. sgRNAs were purified using the MEGAclear Transcription Clean-Up Kit (Invitrogen). Embryos were injected at the 1-cell stage with 1 ng Cas9 (PNA Bio) and 300 pg sgRNA. Following injections, embryos were cultivated at room temperature. To confirm genome editing, direct sequencing of PCR products was applied. DNAs from pools of 10 stage 45 embryos were isolated and gene-specific primers were used to amplify targeted *cfap206* sequences. Genome editing efficiency was calculated using Synthego ICE (https://tools.synthego.com/#/).

High-speed video microscopy of larval epidermal cilia

Control or crispant stage 32 embryos were analysed for epidermal ciliary beating patterns. Specimens were placed into a rectangular chamber constructed from duct tape that was mounted on a slide. Ciliary beating was recorded for 1 s at the ventral-most aspect of the embryo using high-speed Hamamatsu video camera Orca flash 4.0 at 800 fps (frames per second). For analysis of ciliary flow, fluorescent beads of 1 µm diameter (Invitrogen FluoSpheres; 1:2000) were added to the culture medium. Embryos were imaged using a Zeiss Axiocam HSm camera at 175 fps. Evaluation of CBF and ciliary flow was as described above in the respective mouse section.

Acknowledgements

We thank S. Brody (Washington University, St Louis, MO, USA) for *Foxj1* mutant mice, M. Menon and M. Gaestel (Institute for Physiological Chemistry, MHH, Hannover, Germany) for anti-SEPTIN7 antibody; D. Conrad, C. Schippert and P. Hillemanns (Department of Gynaecology and Obstetrics, MHH, Hannover, Germany) for the access to the CASA instrument and their help; and R. Bauerfeind for help with monitoring tracheal cilia. We thank A. Heiser for his assistance with mice care and genotyping.

Competing interests

The authors declare no competing or financial interests.

Author contributions

Conceptualization: A.B., L.T., T.O., M.B., A.G.; Methodology: A.B., K.S.-G., L.T., T.O., J.H., K.B.; Formal analysis: A.B., C.A., L.T., T.O., F.F., J.H., K.B., K.S., E.R., M.B., A.G.; Investigation: A.B., K.S.-G., L.T., T.O., F.F., J.H., K.B., K.S., E.R., L.A.; Resources: E.K.; Writing - original draft: A.B., L.T., M.B., A.G.; Writing - review & editing: A.B., C.A., K.S.-G., L.T., T.O., F.F., J.H., K.B., K.S., E.R., L.A., E.K., M.U.; Supervision: M.U., M.B., A.G.; Project administration: M.B., A.G.; Funding acquisition: M.B., A.G.

Funding

This work was financially supported by the Deutsche Forschungsgemeinschaft (GO 449/14-1 and BL285/14-1) and by the Deutsche Forschungsgemeinschaft Cluster of Excellence 'REBIRTH' to A.G. T.O. was supported by a PhD fellowship from the Landesgraduiertenförderung Baden-Württemberg.

Data availability

The full mass spectrometry proteomics data have been deposited with the ProteomeXchange Consortium via the PRIDE (Vizcaíno et al., 2016) partner repository under the dataset identifier PXD018554.

Supplementary information

Supplementary information available online at
http://dev.biologists.org/lookup/doi/10.1242/dev.188052.supplemental

Peer review history
The peer review history is available online at
https://dev.biologists.org/lookup/doi/10.1242/dev.188052.reviewer-comments.pdf

References

Abdelhamed, Z., Vuong, S. M., Hill, L., Shula, C., Timms, A., Beier, D., Campbell, K., Mangano, F. T., Stottmann, R. W. and Goto, J. (2018). A mutation in Ccdc39 causes neonatal hydrocephalus with abnormal motile cilia development in mice. *Development* **145**, dev154500. doi:10.1242/dev.154500

Afzelius, B. A. and Eliasson, R. (1983). Male and female infertility problems in the immotile-cilia syndrome. *Eur. J. Respir. Dis. Suppl.* **127**, 144-147.

Alten, L., Schuster-Gossler, K., Beckers, A., Groos, S., Ulmer, B., Hegermann, J., Ochs, M. and Gossler, A. (2012). Differential regulation of node formation, nodal ciliogenesis and cilia positioning by Noto and Foxj1. *Development* **139**, 1276-1284. doi:10.1242/dev.072728

Arnaiz, O., Malinowska, A., Klotz, C., Sperling, L., Dadlez, M., Koll, F. and Cohen, J. (2009). Cildb: a knowledgebase for centrosomes and cilia. *Database (Oxford)* **2009**, bap022. doi:10.1093/database/bap022

Banizs, B., Pike, M. M., Millican, C. L., Ferguson, W. B., Komlosi, P., Sheetz, J., Bell, P. D., Schwiebert, E. M. and Yoder, B. K. (2005). Dysfunctional cilia lead to altered ependyma and choroid plexus function, and result in the formation of hydrocephalus. *Development* **132**, 5329-5339. doi:10.1242/dev.02153

Beckers, A., Ott, T., Schuster-Gossler, K., Boldt, K., Alten, L., Ueffing, M., Blum, M. and Gossler, A. (2018). The evolutionary conserved FOXJ1 target gene Fam183b is essential for motile cilia in Xenopus but dispensable for ciliary function in mice. *Sci. Rep.* **8**, 14678. doi:10.1038/s41598-018-33045-2

Blum, M. and Ott, T. (2018). Animal left–right asymmetry. *Curr. Biol.* **28**, R301-R304. doi:10.1016/j.cub.2018.02.073

Brody, S. L., Yan, X. H., Wuerffel, M. K., Song, S.-K. and Shapiro, S. D. (2000). Ciliogenesis and left-right axis defects in forkhead factor HFH-4-null mice. *Am. J. Respir. Cell Mol. Biol.* **23**, 45-51. doi:10.1165/ajrcmb.23.1.4070

Burgoyne, T., Lewis, A., Dewar, A., Luther, P., Hogg, C., Shoemark, A. and Dixon, M. (2014). Characterizing the ultrastructure of primary ciliary dyskinesia transposition defect using electron tomography. *Cytoskeleton (Hoboken)* **71**, 294-301. doi:10.1002/cm.21171

Castleman, V. H., Romio, L., Chodhari, R., Hirst, R. A., de Castro, S. C. P., Parker, K. A., Ybot-Gonzalez, P., Emes, R. D., Wilson, S. W., Wallis, C. et al. (2009). Mutations in radial spoke head protein genes RSPH9 and RSPH4A cause primary ciliary dyskinesia with central-microtubular-pair abnormalities. *Am. J. Hum. Genet.* **84**, 197-209. doi:10.1016/j.ajhg.2009.01.011

Chen, J., Knowles, H. J., Hebert, J. L. and Hackett, B. P. (1998). Mutation of the mouse hepatocyte nuclear factor/forkhead homologue 4 gene results in an absence of cilia and random left-right asymmetry. *J. Clin. Invest.* **102**, 1077-1082. doi:10.1172/JCI4786

Choksi, S. P., Lauter, G., Swoboda, P. and Roy, S. (2014). Switching on cilia: transcriptional networks regulating ciliogenesis. *Development* **141**, 1427-1441. doi:10.1242/dev.074666

Cox, J. and Mann, M. (2008). MaxQuant enables high peptide identification rates, individualized p.p.b.-range mass accuracies and proteome-wide protein quantification. *Nat. Biotechnol.* **26**, 1367-1372. doi:10.1038/nbt.1511

Cox, J., Matic, I., Hilger, M., Nagaraj, N., Selbach, M., Olsen, J. V. and Mann, M. (2009). A practical guide to the MaxQuant computational platform for SILAC-based quantitative proteomics. *Nat. Protoc.* **4**, 698-705. doi:10.1038/nprot.2009.36

de Vries, W. N., Binns, L. T., Fancher, K. S., Dean, J., Moore, R., Kemler, R. and Knowles, B. B. (2000). Expression of Cre recombinase in mouse oocytes: a means to study maternal effect genes. *Genesis* **26**, 110-112. doi:10.1002/(SICI)1526-968X(200002)26:2<110::AID-GENE2>3.0.CO;2-8

Dubaissi, E. and Papalopulu, N. (2011). Embryonic frog epidermis: a model for the study of cell-cell interactions in the development of mucociliary disease. *Dis. Model. Mech.* **4**, 179-192. doi:10.1242/dmm.006494

Edelbusch, C., Cindrić, S., Dougherty, G. W., Loges, N. T., Olbrich, H., Rivlin, J., Wallmeier, J., Pennekamp, P., Amirav, I. and Omran, H. (2017). Mutation of serine/threonine protein kinase 36 (STK36) causes primary ciliary dyskinesia with a central pair defect. *Hum. Mutat.* **38**, 964-969. doi:10.1002/humu.23261

El-Brolosy, M. A., Kontarakis, Z., Rossi, A., Kuenne, C., Günther, S., Fukuda, N., Kikhi, K., Boezio, G. L. M., Takacs, C. M., Lai, S.-L. et al. (2019). Genetic compensation triggered by mutant mRNA degradation. *Nature* **568**, 193-197. doi:10.1038/s41586-019-1064-z

Francis, R. and Lo, C. (2013). Ex vivo method for high resolution imaging of cilia motility in rodent airway epithelia. *J. Vis. Exp.* **78**, e50343. doi:10.3791/50343

Frommer, A., Hjeij, R., Loges, N. T., Edelbusch, C., Jahnke, C., Raidt, J., Werner, C., Wallmeier, J., Große-Onnebrink, J., Olbrich, H. et al. (2015). Immunofluorescence analysis and diagnosis of primary ciliary dyskinesia with radial spoke defects. *Am. J. Respir. Cell Mol. Biol.* **53**, 563-573. doi:10.1165/rcmb.2014-0483OC

Gherman, A., Davis, E. E. and Katsanis, N. (2006). The ciliary proteome database: an integrated community resource for the genetic and functional dissection of cilia. *Nat. Genet.* **38**, 961-962. doi:10.1038/ng0906-961

Gloeckner, C. J., Boldt, K. and Ueffing, M. (2009). Strep/FLAG tandem affinity purification (SF-TAP) to study protein interactions. *Curr. Protoc. Protein Sci.* **57**, 19.20.1-19.20.19. doi:10.1002/0471140864.ps1920s57

Gupta, A., Diener, D. R., Sivadas, P., Rosenbaum, J. L. and Yang, P. (2012). The versatile molecular complex component LC8 promotes several distinct steps of flagellar assembly. *J. Cell Biol.* **198**, 115-126. doi:10.1083/jcb.201111041

Guzman, R. E., Alekov, A. K., Filippov, M., Hegermann, J. and Fahlke, C. (2014). Involvement of ClC-3 chloride/proton exchangers in controlling glutamatergic synaptic strength in cultured hippocampal neurons. *Front. Cell Neurosci.* **8**, 143. doi:10.3389/fncel.2014.00143

Hall, E. A., Keighren, M., Ford, M. J., Davey, T., Jarman, A. P., Smith, L. B., Jackson, I. J. and Mill, P. (2013). Acute versus chronic loss of mammalian Azi1/Cep131 results in distinct ciliary phenotypes. *PLoS Genet.* **9**, e1003928. doi:10.1371/journal.pgen.1003928

Hayes, J. M., Kim, S. K., Abitua, P. B., Park, T. J., Herrington, E. R., Kitayama, A., Grow, M. W., Ueno, N. and Wallingford, J. B. (2007). Identification of novel ciliogenesis factors using a new in vivo model for mucociliary epithelial development. *Dev. Biol.* **312**, 115-130. doi:10.1016/j.ydbio.2007.09.031

Hirokawa, N., Tanaka, Y., Okada, Y. and Takeda, S. (2006). Nodal flow and the generation of left-right asymmetry. *Cell* **125**, 33-45. doi:10.1016/j.cell.2006.03.002

Huizar, R. L., Lee, C., Boulgakov, A. A., Horani, A., Tu, F., Marcotte, E. M., Brody, S. L. and Wallingford, J. B. (2018). A liquid-like organelle at the root of motile ciliopathy. *eLife* **7**, 4154. doi:10.7554/eLife.38497

Ibañez-Tallon, I., Pagenstecher, A., Fliegauf, M., Olbrich, H., Kispert, A., Ketelsen, U.-P., North, A., Heintz, N. and Omran, H. (2004). Dysfunction of axonemal dynein heavy chain Mdnah5 inhibits ependymal flow and reveals a novel mechanism for hydrocephalus formation. *Hum. Mol. Genet.* **13**, 2133-2141. doi:10.1093/hmg/ddh219

Ikegami, K., Sato, S., Nakamura, K., Ostrowski, L. E. and Setou, M. (2010). Tubulin polyglutamylation is essential for airway ciliary function through the regulation of beating asymmetry. *Proc. Natl. Acad. Sci. USA* **107**, 10490-10495. doi:10.1073/pnas.1002128107

Inglis, P. N., Boroevich, K. A. and Leroux, M. R. (2006). Piecing together a ciliome. *Trends Genet.* **22**, 491-500. doi:10.1016/j.tig.2006.07.006

Jacquet, B. V., Salinas-Mondragon, R., Liang, H., Therit, B., Buie, J. D., Dykstra, M., Campbell, K., Ostrowski, L. E., Brody, S. L. and Ghashghaei, H. T. (2009). FoxJ1-dependent gene expression is required for differentiation of radial glia into ependymal cells and a subset of astrocytes in the postnatal brain. *Development* **136**, 4021-4031. doi:10.1242/dev.041129

Jain, R., Pan, J., Driscoll, J. A., Wisner, J. W., Huang, T., Gunsten, S. P., You, Y. and Brody, S. L. (2010). Temporal relationship between primary and motile ciliogenesis in airway epithelial cells. *Am. J. Respir. Cell Mol. Biol.* **43**, 731-739. doi:10.1165/rcmb.2009-0328OC

Knowles, M. R., Ostrowski, L. E., Leigh, M. W., Sears, P. R., Davis, S. D., Wolf, W. E., Hazucha, M. J., Carson, J. L., Olivier, K. N., Sagel, S. D. et al. (2014). Mutations in RSPH1 cause primary ciliary dyskinesia with a unique clinical and ciliary phenotype. *Am. J. Respir. Crit. Care. Med.* **189**, 707-717. doi:10.1164/rccm.201311-2047OC

Kremer, J. R., Mastronarde, D. N. and McIntosh, J. R. (1996). Computer visualization of three-dimensional image data using IMOD. *J. Struct. Biol.* **116**, 71-76. doi:10.1006/jsbi.1996.0013

Lee, L. (2013). Riding the wave of ependymal cilia: genetic susceptibility to hydrocephalus in primary ciliary dyskinesia. *J. Neurosci. Res.* **91**, 1117-1132. doi:10.1002/jnr.23238

Lin, J., Tritschler, D., Song, K., Barber, C. F., Cobb, J. S., Porter, M. E. and Nicastro, D. (2011). Building blocks of the nexin-dynein regulatory complex in Chlamydomonas flagella. *J. Biol. Chem.* **286**, 29175-29191. doi:10.1074/jbc.M111.241760

Lindemann, C. B. and Lesich, K. A. (2010). Flagellar and ciliary beating: the proven and the possible. *J. Cell Sci.* **123**, 519-528. doi:10.1242/jcs.051326

Lucas, J. S., Davis, S. D., Omran, H. and Shoemark, A. (2019). Primary ciliary dyskinesia in the genomics age. *Lancet Respir Med.* **8**, 202-216. doi:10.1016/S2213-2600(19)30374-1

Lyons, R. A., Saridogan, E. and Djahanbakhch, O. (2006). The reproductive significance of human Fallopian tube cilia. *Hum. Reprod. Update* **12**, 363-372. doi:10.1093/humupd/dml012

Moorman, A. F. M., Houweling, A. C., de Boer, P. A. J. and Christoffels, V. M. (2001). Sensitive nonradioactive detection of mRNA in tissue sections: novel application of the whole-mount in situ hybridization protocol. *J. Histochem. Cytochem.* **49**, 1-8. doi:10.1177/002215540104900101

Moreno-Mateos, M. A., Vejnar, C. E., Beaudoin, J.-D., Fernandez, J. P., Mis, E. K., Khokha, M. K. and Giraldez, A. J. (2015). CRISPRscan: designing highly efficient sgRNAs for CRISPR-Cas9 targeting in vivo. *Nat Meth* **12**, 982-988. doi:10.1038/nmeth.3543

Mukherjee, I., Roy, S. and Chakrabarti, S. (2019). Identification of important effector proteins in the FOXJ1 transcriptional network associated with ciliogenesis and ciliary function. *Front. Genet.* **10**, 23. doi:10.3389/fgene.2019.00023

Nieuwkoop, P. D. and Faber, J. (1994). *Normal Table of Xenopus laevis (Daudin): A Systematical and Chronological Survey of the Development from the Fertilized Egg till the End of Metamorphosis*. New York: Garland Publishing Inc.

Nonaka, S., Tanaka, Y., Okada, Y., Takeda, S., Harada, A., Kanai, Y., Kido, M. and Hirokawa, N. (1998). Randomization of left-right asymmetry due to loss of nodal cilia generating leftward flow of extraembryonic fluid in mice lacking KIF3B motor protein. *Cell* **95**, 829-837. doi:10.1016/S0092-8674(00)81705-5

Olsen, J. V., de Godoy, L. M. F., Li, G., Macek, B., Mortensen, P., Pesch, R., Makarov, A., Lange, O., Horning, S. and Mann, M. (2005). Parts per million mass accuracy on an Orbitrap mass spectrometer via lock mass injection into a C-trap. *Mol. Cell Proteomics* **4**, 2010-2021. doi:10.1074/mcp.T500030-MCP200

Osinka, A., Poprzeczko, M., Zielinska, M. M., Fabczak, H., Joachimiak, E. and Wloga, D. (2019). Ciliary proteins: filling the gaps. recent advances in deciphering the protein composition of motile ciliary complexes. *Cells* **8**, 730. doi:10.3390/cells8070730

Praveen, K., Davis, E. E. and Katsanis, N. (2015). Unique among ciliopathies: primary ciliary dyskinesia, a motile cilia disorder. *F1000Prime Rep.* **7**, 36. doi:10.12703/P7-36

Rachev, E., Schuster-Gossler, K., Fuhl, F., Ott, T., Tveriakhina, L., Beckers, A., Hegermann, J., Boldt, K., Mai, M., Kremmer, E. et al. (2020). CFAP43 modulates ciliary beating in mouse and Xenopus. *Dev. Biol.* **459**, 109-125. doi:10.1016/j.ydbio.2019.12.010

Reynolds, M. J., Phetruen, T., Fisher, R. L., Chen, K., Pentecost, B. T., Gomez, G., Ounjai, P. and Sui, H. (2018). The developmental process of the growing motile ciliary tip region. *Sci. Rep.* **8**, 7977. doi:10.1038/s41598-018-26111-2

Rodríguez, C. I., Buchholz, F., Galloway, J., Sequerra, R., Kasper, J., Ayala, R., Stewart, A. F. and Dymecki, S. M. (2000). High-efficiency deleter mice show that FLPe is an alternative to Cre-loxP. *Nat. Genet.* **25**, 139-140. doi:10.1038/75973

Rossi, A., Kontarakis, Z., Gerri, C., Nolte, H., Hölper, S., Krüger, M. and Stainier, D. Y. R. (2015). Genetic compensation induced by deleterious mutations but not gene knockdowns. *Nature* **524**, 230-233. doi:10.1038/nature14580

Rudat, C., Grieskamp, T., Röhr, C., Airik, R., Wrede, C., Hegermann, J., Herrmann, B. G., Schuster-Gossler, K. and Kispert, A. (2014). Upk3b is dispensable for development and integrity of urothelium and mesothelium. *PLoS ONE* **9**, e112112. doi:10.1371/journal.pone.0112112

Satir, P., Heuser, T. and Sale, W. S. (2014). A structural basis for how motile cilia beat. *Bioscience* **64**, 1073-1083. doi:10.1093/biosci/biu180

Shinohara, K., Chen, D., Nishida, T., Misaki, K., Yonemura, S. and Hamada, H. (2015). Absence of radial spokes in mouse node cilia is required for rotational movement but confers ultrastructural instability as a trade-off. *Dev. Cell* **35**, 236-246. doi:10.1016/j.devcel.2015.10.001

Sivadas, P., Dienes, J. M., St. Maurice, M., Meek, W. D. and Yang, P. (2012). A flagellar A-kinase anchoring protein with two amphipathic helices forms a structural scaffold in the radial spoke complex. *J. Cell Biol.* **199**, 639-651. doi:10.1083/jcb.201111042

Sive, H. L., Grainger, H. M. and Harland, R. M. (2000). *Early Development of Xenopus Laevis: A Laboratory Manual*. Cold Spring Harbor: Cold Spring Harbor Laboratory Press.

Soares, H., Carmona, B., Nolasco, S., Viseu Melo, L. and Gonçalves, J. (2019). Cilia distal domain: diversity in evolutionarily conserved structures. *Cells* **8**, 160. doi:10.3390/cells8020160

Spassky, N., Merkle, F. T., Flames, N., Tramontin, A. D., García-Verdugo, J. M. and Alvarez-Buylla, A. (2005). Adult ependymal cells are postmitotic and are derived from radial glial cells during embryogenesis. *Neurosci* **25**, 10-18. doi:10.1523/JNEUROSCI.1108-04.2005

Stannard, W. and O'Callaghan, C. (2006). Ciliary function and the role of cilia in clearance. *J. Aerosol Med.* **19**, 110-115. doi:10.1089/jam.2006.19.110

Stauber, M., Weidemann, M., Dittrich-Breiholz, O., Lobschat, K., Alten, L., Mai, M., Beckers, A., Kracht, M. and Gossler, A. (2017). Identification of FOXJ1 effectors during ciliogenesis in the foetal respiratory epithelium and embryonic left-right organiser of the mouse. *Dev. Biol.* **423**, 170-188. doi:10.1016/j.ydbio.2016.11.019

Takeda, S. and Narita, K. (2012). Structure and function of vertebrate cilia, towards a new taxonomy. *Differentiation* **83**, S4-S11. doi:10.1016/j.diff.2011.11.002

Tyanova, S., Temu, T., Sinitcyn, P., Carlson, A., Hein, M. Y., Geiger, T., Mann, M. and Cox, J. (2016). The Perseus computational platform for comprehensive analysis of (prote)omics data. *Nat. Meth.* **13**, 731-740. doi:10.1038/nmeth.3901

Vasudevan, K. K., Song, K., Alford, L. M., Sale, W. S., Dymek, E. E., Smith, E. F., Hennessey, T., Joachimiak, E., Urbanska, P., Wloga, D. et al. (2015). FAP206 is a microtubule-docking adapter for ciliary radial spoke 2 and dynein c. *Mol. Biol. Cell* **26**, 696-710. doi:10.1091/mbc.E14-11-1506

Vizcaíno, J. A., Csordas, A., del-Toro, N., Dianes, J. A., Griss, J., Lavidas, I., Mayer, G., Perez-Riverol, Y., Reisinger, F., Ternent, T. et al. (2016). 2016 update of the PRIDE database and its related tools. *Nucleic. Acids Res.* **44**, D447-D456. doi:10.1093/nar/gkv1145

Walentek, P. and Quigley, I. K. (2017). What we can learn from a tadpole about ciliopathies and airway diseases: using systems biology in Xenopus to study cilia and mucociliary epithelia. *Genesis* **55**, e23001. doi:10.1002/dvg.23001

Wallmeier, J., Frank, D., Shoemark, A., Nöthe-Menchen, T., Cindrić, S., Olbrich, H., Loges, N. T., Aprea, I., Dougherty, G. W., Pennekamp, P. et al. (2019). De novo mutations in FOXJ1 result in a motile ciliopathy with hydrocephalus and randomization of left/right body asymmetry. *Am. J. Hum. Genet.* **105**, 1030-1039. doi:10.1016/j.ajhg.2019.09.022

Weidemann, M., Schuster-Gossler, K., Stauber, M., Wrede, C., Hegermann, J., Ott, T., Boldt, K., Beyer, T., Serth, K., Kremmer, E. et al. (2016). CFAP157 is a murine downstream effector of FOXJ1 that is specifically required for flagellum morphogenesis and sperm motility. *Development* **143**, 4736-4748. doi:10.1242/dev.139626

Zhang, S. and Mitchell, B. J. (2016). Basal bodies in Xenopus. *Cilia* **5**, 2-6. doi:10.1186/s13630-016-0024-6

Zhu, L., Liu, H., Chen, Y., Yan, X. and Zhu, X. (2019). Rsph9 is critical for ciliary radial spoke assembly and central pair microtubule stability. *Biol. Cell* **111**, 29-38. doi:10.1111/boc.201800060

Ziętkiewicz, E., Bukowy-Bieryłło, Z., Voelkel, K., Klimek, B., Dmeńska, H., Pogorzelski, A., Sulikowska-Rowińska, A., Rutkiewicz, E. and Witt, M. (2012). Mutations in radial spoke head genes and ultrastructural cilia defects in East-European cohort of primary ciliary dyskinesia patients. *PLoS ONE* **7**, e33667. doi:10.1371/journal.pone.0033667